Energy
Advances

Accepted Manuscript

This article can be cited before page numbers have been issued, to do this please use: H. Ullah, S. Mortazavi, A. M. Flatae, A. M. Khan and X. Jiang, *Energy Adv.*, 2026, DOI: 10.1039/D6YA00012F.

ROYAL SOCIETY
OF CHEMISTRY

rsc.li/energy-advances

View Article Online
DOI: 10.1039/D6YA00012F

ARTICLE

Scalable fabrication and electrochemical characterization of binder-free Fe_3O_4@C films on Cu Current Collector

Hameed Ullah,*[a] Seyedhossein Mortazavi, [a] Assegid Mengistu Flatae, [b] Asad Muhammad Khan, [c] and Xin Jiang *[a]

Received 00th January 20xx,
Accepted 00th January 20xx

DOI: 10.1039/x0xx00000x

Here we present a scalable strategy for fabrication of nanostructured magnetite (Fe_3O_4) films directly on a copper (Cu) current collector as potential anodes for energy storage devices. Hydrothermal synthesis was employed in first step to realize Fe_3O_4 films which were subsequently encapsulated in carbon shell in a controlled way using chemical vapor deposition (CVD) techniques. Through a systematic investigations, it was revealed that lower hydrothermal temperature (80°C) gives rhombus-shaped nanoarchitectures which were primarily composed of α-FeOOH. At higher temperature (120°C), three-dimensional (3D) superstructures comprising of Fe_3O_4/iron carbonate ($FeCO_3$) composite nanolayers were found. Furthermore, it was revelaed that, irrespective of the composition of hydrothermally synthesized film, each one converted upon calcination to a cubic Fe_3O_4 without any significant changes in the morphology. A conformal carbon encapsulation allowed to form Fe_3O_4@C core–shell structures having tunable shell thicknesses and strong interfacial bonding (Fe-O-C). Although structural investigations showed improvement in crystallinity with carbon encapsulation by either CVD techniques, but it was more pronounced in case of microwave plasma CVD (MP-CVD), which also induced partial reduction of Fe_3O_4 to metallic iron (Fe). The films showed pseudocapacitive behavior in 1M Na_2SO_4 during electrochemical evaluation, and stored charge at lower scan rates predominantly by a diffusion-controlled process, which decreased with increasing scan rate, leading to a dominant capacitive process for charge storage. The developed binder-free films have a great potential as highly robust anodes for lithium and post-lithium ion batteries (LIBs), supercapacitors, and battery-supercapacitor hybrid devices.

Introduction

The demand for environmentally responsible and renewable energy has increased significantly, owing to the escalating demand for rapid electrification of transportation; consequently, the demand for high capacity energy storage systems for large scale applications has intensified during the last couple of years [1–3]. Presently, lithium ion batteries (LIBs) are the preferred energy storage devices owing to their high energy storage density and reliability [3–5]. However, the commercially available LIBs of today rely primarily upon electrode materials which are suffered by their intrinsically low theoretical specific capacities [5]. For example, the main anode material *i.e.,* graphite has a theoretical specific capacity of 372 $mAhg^{-1}$ which is already achieved [6]. It is, therefore, unrealistic to look towards these materials for their implementation in LIBs having the potential to fully meet future requirements of the extended range and high power applications [7–9]. Owing to these facts, it is need of the time to develop alternative anode materials, having high specific capacities, low cost, environmental accountability and robustness compared to the conventional graphite-based anodes [10].

Transition metal oxides (TMOs) are decorated with nearly all these characteristics, and therefore, attracted significant research attention. While operating via conversion reaction mechanism, majority of them, TMOs have the capabilities to deliver specific capacities many times higher than the graphite-based anodes owing to their utilization of multiple oxidation states [11,12]. Among the TMOs, magnetite (Fe_3O_4) is particularly interesting as electrode material for energy storage devices owing to its high theoretical capacity of ~920 $mAhg^{-1}$, environmental benignity, abundance, and cost-effectiveness [13]. Fe_3O_4 is highly versatile as an energy storage material, showing extended potential as electrode material not only for LIBs but in some of the emerging energy storage technologies like post-LIBs and supercapacitors [14–17].

Despite all these advantages, Fe_3O_4 anodes could not pave their way towards large scale implementation in practical energy storage devices owing to their fundamental challenges which are intrinsic to nearly all conversion-type electrode materials. Two of these challenges *i.e.,* extreme volume changes during conversion and low electrical conductivities are particularly significant to be considered while designing and developing the electrode materials. First, the volume change during metalation/demetalation is massive (>200%), leading to significant mechanical stress which causes active material pulverization, electrical isolation, and continuous fracturing of the solid electrolyte interphase (SEI) layer [18–20]. Second, the intrinsically low electrical conductivity of Fe_3O_4 is responsible for restricting the electron transport kinetics on one hand, and on the other hand, limiting the rate capability [21]. Additionally, these issues are further

---

[a] *Address here.*
[b] *Address here.*
[c] *Address here.*
† Footnotes relating to the title and/or authors should appear here.
Supplementary Information available: [details of any supplementary information available should be included here]. See DOI: 10.1039/x0xx00000x

View Article Online
DOI: 10.1039/D5YA00012F

aggravated in the traditional slurry based electrode fabrications by the polymer binders and conductive additives as they are responsible for introduction of inactive mass/volume on one hand, and on the other hand, rely on the weak van der Waals forces between the material and the current collector [14,22,23].

The issues related to the binders could be overcome by growing the active materials directly onto the current collector through an effective strategy to realize binder-free electrodes [24–26]. The architectures which are engineered this way help in ensuring of robust electrical contact on one hand, and on the other hand, help in eliminating of inactive weights of the resulting electrodes [26]. Additionally, if included during fabrication, the open porous structure accommodates effectively the strain produced during cycling [26]. This strategy have been previously demonstrated and reported, showing improved performance of hydrothermally grown Fe_3O_4 materials directly onto the substrate [27–29]. However, the intrinsic issue of conductivity and pulverization at the particle level could not be alone resolved through the binder-free approach. The remaining challenges could be effectively overcome by encapsulating the Fe_3O_4 particles of the directly deposited materials on the current collector within a conductive carbon shell [30–32]. A viably designed and robustly engineered carbon shell while acting as physical buffer mitigates the volume changes during cycling on one hand, and on the other hand, provide continuous conductive pathways [33–35]. Of the various techniques and approaches available and employed for this purpose, chemical vapor deposition (CVD) is quite a unique technique with numerous advantages while coating complex three dimensional (3D) architectures. For example, CVD provide uniform and conformal coatings without compromising the original morphology of the underlying particles as it involves a gas-phase process that can penetrate complex pores [36–38].

However, to the best of our knowledge, there is lacking of a systematic investigations of binder-free Fe_3O_4 encapsulation in carbon shell by CVD, and thus a large research and technology gap exists in this regards. Therefore, in our opinion, it is needed to address this gap effectively through a viably designed and robustly executed fabrication strategy. Furthermore, the effect of CVD parameters on the phase, microstructure and morphology of the carbon encapsulated Fe_3O_4 architectures is not well understood, and thus on their electrochemical performance. Therefore, a systematic probing of the CVD parameters influence on the binder-free Fe_3O_4 material properties and its electrochemical performance is critical to be investigated.

Numerous synthesis methods have been explored for preparation of morphology-specific nanoarchitectures. However, realization of Fe_3O_4 directly on the current collector in the desired shape is quite challenging, if not impossible. Despite these challenges, the hydrothermal synthesis method is decorated with more pros than cons, including control over engineering of the desired architecture at nanometer-level scale, for achieving this goal [39]. It is pertinent to mention here that the shape of nanoparticle is critical in dictating the functionalities of the materials [40,41]. For example, rhombus-shaped one-dimensional (1D) nanostructures showed higher electrochemical performance, which was owed to their unique architecture and morphology [42–44]. These unique architectures, *i.e.,* rhombus-shaped 1D nanorods for Fe_3O_4 have not been explored to date, to the best of our knowledge, as loose powder, let alone as binder-free electrode materials directly on the current collector.

Here, we present on the fabrication of binder free Fe_3O_4 films directly on the current collector in the desired morphologies by the so-called hydrothermal synthesis, and carbon encapsulation of these films by two distinct CVD systems including thermal CVD (T-CVD) using acetylene (C_2H_2) gas and microwave plasma enhanced CVD (MP-CVD) using methane (CH_4) gas as carbon sources to investigate the effect of carbon encapsulation on the structure and properties of the resulting nanomaterials. The aim was to demonstrate that the selected method of synthesis of Fe_3O_4, *i.e.,* hydrothermal have the potential to equip us with the ability to tailor the shape of the Fe_3O_4 nanoarchitectures as desired. Furthermore, the aim was to coat the binder-free Fe_3O_4 intricate films without compromising their morphology. Finally, it was aimed to systematically investigate the structure-property relationships by following the fabricated film electrochemically.

Experimental

Materials

All the materials used in this research were purchased from commercial suppliers and used as received unless mentioned otherwise. Copper (Cu) foil (>99.95 %) of 0.1 mm thickness was purchased from Carl Roth GmbH and cleaned by ultrasonication for 10 minutes in distilled water (produced in our own laboratory facility) followed by ethanol (>96 % of VWR Chemicals). The thoroughly cleaned Cu foil was overnight dried in laboratory oven at 60°C. Iron(II) sulfate heptahydrate ($FeSO_4 \cdot 7H_2O$) (>99 %) and Na_2SO_4 (>99 %) of Sigma-Aldrich, urea (99 %) of ThermoFischer and ammonium fluoride (NH_4F) (~96%) of Alfa Aesar were purchased from commercial supplier and used as received.

Hydrothermal processing

Following the reported procedure [26], the solution for hydrothermal processing of Cu foil was prepared by dissolving 5 mmol of $FeSO_4 \cdot 7H_2O$, 15 mmol of urea and 10 mmol of NH_4F into 70 mL of distilled water by stirring at 500 rpm at room temperature. After 10 minutes of stirring, the solution was transferred into a PTFE-lined 125 mL stainless steel autoclave (acid digestion vessel of Parr Instrument (Deutschland) GmbH) along with thoroughly prepared Cu foil which was positioned at 45°. After tightly closing, the vessel was placed in a laboratory oven which was pre-heated to the desired temperature of 80°C (120°C), and maintained for 12 hours. Afterwards, the vessel was allowed to cool down to room temperature naturally. The Cu foil was retrieved, and rinsed with ethanol and distilled water. The loose powder, which were precipitated in the vessel, were recovered by centrifugation at 6000 rpm and cleaned by washing with distilled water and ethanol. Both Cu foil and the powder were dried overnight at 60°C in the laboratory oven, and then calcined at 450°C under nitrogen (N_2) stream (200 sccm) for 4 hours while furnace was heated at a rate of 5°C/min.

Carbon-encapsulation

View Article Online
DOI: 10.1039/D6YA00012F

Carbon encapsulation of the resulting films particles were carried out by CVD techniques including thermal CVD (T-CVD) and MP-CVD. The post-calcination films were inserted into the T-CVD chamber which was then sealed tightly and flushed with dry N_2 for 30 minutes. Afterwards, the chamber was heated at a rate of 5°C/min up to 450°C and then flushed with Ar gas. For coating, a mixture of Ar (80%) and acetylene (C_2H_2, Messer Industriegase GmbH, Germany) (20%) was allowed into the chamber for 30 minutes followed by cooling of it naturally to room temperature. Likewise, MP-CVD was used for the carbon-encapsulation of the films particles. The sample was placed in the MP-CVD chamber which was flushed for 10 minutes with hydrogen (H_2), flowing at rate of 100 sccm and pressure of 15 Torr. Afterwards, CH_4 at 10 sccm flow rate and 19 Torr of pressure was allowed to enter the chamber. The coating was continued for five minutes at microwave power of 500 W during which time the temperature raised to ~450°C.

All the prepared samples are summarized in Table SI-1, showing the sample codes used in this manuscript and the synthesis parameters.

Characterization

The x-ray diffraction (XRD) data were collected by PANalytical Empyrean (XRD) diffractometer which was equipped with Cu Kα (λ = 1.5425 Å) radiations. The data were searched and matched by XPertPro software while Rietveld refinement were carried out by FullProf Suite. Raman spectra were measured using InVita Reflex (Renishaw) equipped with Laser (excitation λ = 656 nm) which was used for continuous perpendicular illumination of the sample. X-rays photoelectron spectroscopy (XPS) measurements were performed on SSX-100 (XPS) spectrometer (Evans Analytical Group LLC) and the data were fitted using CasaXPS software. Scanning electron microscopy (SEM) images were acquired by using Zeiss Ultra 55 (FE-SEM). Energy-dispersive X-ray (EDX) spectroscopy was carried out with a FE-SEM coupled Thermo Scientific detector, and quantitative and qualitative elemental analysis spectra and mapping were acquired. Transmission electron microscopy (TEM) and scanning TEM (STEM) were performed over FEI Talos 200 FA.

Electrochemical measurements

Electrochemical measurements were performed in a conventional three-electrode cell by CHI660E Electrochemical Workstation. A 1 cm x 1 cm piece of the film was used as working electrode. Platinum (Pt) wire was used as counter electrode while Ag/AgCl was used as reference electrode. All the measurement were made in a 1 M Na_2SO_4 solution at room temperature. Cyclic voltammetry (CV) measurements were studied in the potential window of 0 V to -1.0 V at different scanning rates ranging from 5 mV/s to 150 mV/s. For each sample, two cycles were recorded. Electrochemical impedance spectroscopy (EIS) measurements were carried out at open circuit potential in the frequency range of 10 kHz – 0.01 Hz while keeping the AC perturbation amplitude of 5 mV.

Results and discussion

The samples were prepared with the aim to fabricate Fe_3O_4 films directly on the current collector *i.e.,* Cu for applications as negative electrode (anode) in solid state batteries. As anticipated, the material deposits on the Cu substrate as film, while the excess settles down as powder. The powder as well as film were retrieved and characterized by powder XRD. The pre- and post-calcination XRD patterns of the powder received at the end of hydrothermal process carried out at 80°C are presented in **Fig. 1(a)**, showing distinct diffraction peaks. However, the position and intensities of the peaks are different for the pre- and post-calcination powder, indicating that the crystalline phase and composition of the as received powder has changed upon calcination. Peaks in the XRD pattern of pre-calcination powder were searched and matched using XpertPro and found that the powder is composed of iron oxy-hydroxide (FeOOH). The main intensity peaks match with standard XRD pattern of β-FeOOH given by the powder diffraction file (PDF) [01-075-1594] in the inorganic crystal structure database (ICSD). A small fraction of peaks was found, matching the standard XRD pattern of α-FeOOH (PDF: [00-017-0536]), indicating the fact that the FeOOH powder crystallizes in two phases in which β-FeOOH is the majority while α-FeOOH is the minority phase. The post-calcination XRD pattern shown in **Fig. 1(a)** was searched and the peaks were matched with standard XRD pattern of cubic Fe_3O_4 given by PDF [01-076-1849]. From the XRD data it is obvious that the FeOOH decomposes upon heating under the applied conditions and converts to Fe_3O_4 according to the following proposed decomposition reaction (Eq. 1).

$$12FeOOH \xrightarrow{Heating} 4Fe_3O_4 + 6H_2O + O_2 \qquad (1)$$

Furthermore, it is evident that the transformation of FeOOH to Fe_3O_4 completes under the applied conditions, as no other phase is shown by the XRD pattern of the post-calcination powder.

XRD pattern of the film deposited directly on Cu substrate through hydrothermal processing at 80°C is presented **Fig. 1(b)**, showing distinct diffraction peaks at various 2θ. The intense peaks at 2θ of 43.29°, 50.42° and 74.11° correspond to the diffraction peaks of Cu substrate as per matching with the standard XRD pattern given in ICSD by PDF [01-085-1326] and the uncoated Cu substrate XRD pattern which is presented in **Fig. SI-1**. The rest of the diffraction peaks were searched and matched by XpertPro, and found that they match well with standard XRD pattern of α-FeOOH which is given by PDF [01-081-0462] in ICSD. Contrary to the settled down powder which were mostly composed of β-FeOOH, the film is comprising of α-FeOOH. Like powder, the as fabricated film by hydrothermal treatment at 80°C converts to Fe_3O_4 which is confirmed by the XRD pattern presented in **Fig. 1(b)**, showing intense diffraction peaks which match exactly with the standard PDF [01-076-1849] of cubic Fe_3O_4. The post-calcination film on Cu substrate was subjected to carbon coating of the Fe_3O_4 material by thermal CVD, and the pertinent XRD pattern is presented in **Fig. 1(b)**. In comparison to the pre-carbon-coated film, XRD pattern of the post-carbon-coated film appears with some visible changes. A hump superimposed with a diffraction peak of Fe_3O_4 appears in 2θ range of 15° to 25°. Secondly, the intensity of Fe_3O_4 peaks decreases. However, the peaks upon search and match corresponds to the reflection of standard XRD pattern given by PDF [01-076-1849] of Fe_3O_4. This indicates that the film material is crystalline, and the phase and composition remained unchanged after coating with carbon. The changes including appearance of the hump and the decrease in intensity of Fe_3O_4 peaks could be corresponded to the presence of amorphous carbon. The XRD pattern in **Fig. 1(b)** of the film coated with carbon by MP-CVD

View Article Online
DOI: 10.1039/D6YA00012E

tells a different story. Like the XRD pattern of carbon-coated film by thermal CVD, the MP-CVD carbon-coated film shows a broad hump in 2θ range of 15° to 30°. The search and match of the XRD pattern by XpertPro show that the basic crystalline structure remain unchanged *i.e.,* the film is composed of Fe_3O_4 as the pre-carbon-coated film was. However, contrary to the thermal CVD carbon-coated film, intensity of Fe_3O_4 peaks increased significantly, indicating an improvement in the crystal quality. Furthermore, new peaks in addition to those of Fe_3O_4 and Cu substrate appeared at 2θ of 44.63° and 64.87°. Upon search and match it was found that these very peaks match with the standard XRD pattern of iron (Fe) given by PDF [01-087-0721] in the ICSD. It means that the Fe_3O_4 film upon subjecting to carbon coating by MP-CVD underwent reduction, though partially.

XRD patterns of the pre- and post-calcination powder sample retrieved from autoclave which was heat treated at 120°C for fabrication of film on the Cu substrate are presented in **Fig. 1(c)**. Diffractogram of the as received powder sample shows distinct diffraction peaks which were searched and matched by XpertPro with the standard XRD pattern of cubic Fe_3O_4 given by PDF [01-076-1849] in ICSD. A second set of lower intensity reflections at 2θ of 24.62°, 31.97°, 38.09°, 46.15°, 50.99°, 52.79° *etc.* was found besides the diffraction peaks of Fe_3O_4. After search and match by XpertPro with standard XRD pattern given by PDF [00-003-0746], it was found that these peaks are owed to the reflections from crystal planes of iron carbonate ($FeCO_3$). The post-calcination XRD pattern of the powder retrieved from autoclave of the hydrothermal process carried out at 120°C is presented in **Fig. 1(c)**, showing distinct peaks which were searched and matched with standard XRD pattern (PDF: [01-076-1849]) of cubic Fe_3O_4. This indicates that under the given calcination regime, the powder comprising of Fe_3O_4 and $FeCO_3$ were converted to a single phase material *i.e.,* Fe_3O_4 according to the following proposed decomposition reaction of $FeCO_3$ (Eq. 2).

$$6FeCO_3 \xrightarrow{Calcination} 2Fe_3O_4 + C + 5CO_2 \tag{2}$$

Besides the peaks of Fe_3O_4 phase, no other peaks are shown by the XRD pattern of post-calcination powder sample.

The films fabricated on Cu substrate by hydrothermal processing at 120°C were characterized by powder XRD and the pertinent diffractograms are presented in **Fig. 1(d)**. The as fabricated film gives well established peaks in its XRD pattern for the Cu substrate and the coating on it. Upon search and match by XpertPro, the peaks other than those of Cu substrate are the result of reflections from crystallographic planes of Fe_3O_4 and $FeCO_3$ as these peaks match very well with the standard XRD patterns of cubic Fe_3O_4 and Rhombohedral $FeCO_3$ which are given, respectively, by PDF [01-076-1849] and [00-003-0746] in ICSD. Contrary to the powder sample, film has higher amount of $FeCO_3$. Upon calcination of the as received film, the crystal quality improved significantly which is evident from the intensity and narrowing of the peaks in the XRD pattern of the post-calcination film presented in **Fig. 1(d)**. The peaks were searched and matched by XpertPro, and found that the film is composed of a single phase *i.e.,* Fe_3O_4 as the reflections match very well with the stand XRD pattern of Fe_3O_4 given by PDF [01-079-0418] in ICSD. The XRD pattern of the post-calcination films after coating with carbon by thermal CVD is presented in **Fig. 1(d)**. The peaks match with a single phase *i.e.,* cubic Fe_3O_4 given by PDF [01-079-0418] from the ICSD. However, the peaks intensity is lower after coating with carbon which is also shown by a broad hump in the XRD pattern as amorphous material. The film coated with carbon by MP-CVD gives peaks which match with standard XRD pattern in PDF [01-075-1372] of cubic Fe_3O_4. However, the diffractogram gives also peaks for a second phase which is matched with PDF [00-006-0696] in ICSD of cubic Fe. A hump superimposed with peaks of Fe_3O_4 phase is also given by the XRD pattern, indicating the presence of amorphous carbon.

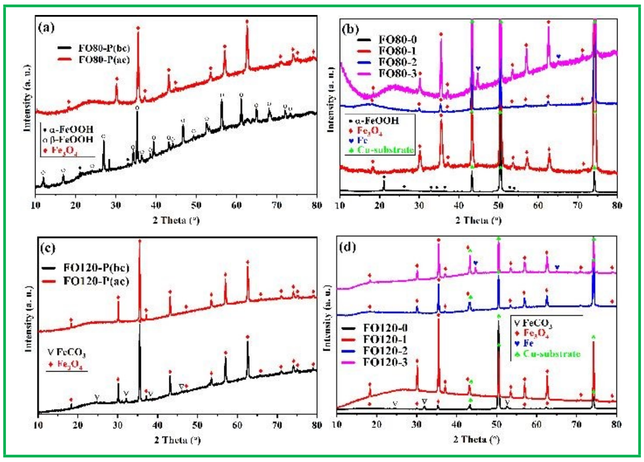

Fig. 1. Powder XRD patterns of the pre- and post-calcined powder obtained by hydrothermal processing at 80°C (a) and 120°C (c), and films deposited on Cu-substrate by hydrothermal processing at 80°C (a) and 120°C (b), and subsequently coated with carbon by thermal and microwave plasma CVD.

Rietveld refinement of the samples (residual powder and films) was carried out by employing the Rietveld's whole-profile fitting method using FullProf software [45], and the pertinent XRD patterns with Rietveld refined data are presented in supplementary information (SI). In the refined XRD patterns presented in SI, the Bragg's peak positions are given by vertical lines, the line of difference between the observed and the calculated intensities is presented at the bottom of the corresponding patterns, the observed intensity is given by open circles and the refined/calculated intensity by Rietveld refinement is given as solid line superimposed over the measured XRD pattern. The reflection peaks are labelled with the corresponding lattice planes. Pseudo-Voigt analytical function given in Table SI-2 and 5 was used for fitting the experimental diffraction profiles as it has certain advantages discussed elsewhere [46]. The refinement steps involve refinement of the parameters in the following order unless stated otherwise: scale factor, zero point of detector, background which was fixed by using linear interpolation between a set of points provided, lattice constants, atomic positions unless stated otherwise, peak shape and symmetry parameters, atom occupancies unless stated otherwise and overall temperature factor. The quality of refinement was quantified from the figures of merit, including R_p (pattern residual), R_{wp} (weighted pattern residual), R_{exp} (expected pattern residual), R_B (Bragg's factor), R_F (structural factor) and goodness of fit (χ^2), for which the mathematical relations are numerously reported in the published literature [47]. Values of the above mentioned reliability factors for all the samples are presented Table SI-2 and 5. Refinement was continued till achieving of convergence and goodness of fit (GOF =

View Article Online
DOI: 10.1039/D6YA00012F

R_{wp}/R_{exp}) close to 1. It is pertinent to mention here that each time the data were plotted and the convergence/fitting of refined pattern with the measured one was visually observed.

XRD pattern of the residual powder (labelled as FO80-P$_{(bc)}$) retrieved from autoclave which was subjected to heating at 80°C was refined and is presented in **Fig. SI-2 (a)**, showing a very good fitting. The refined parameters like crystal axes and the crystal axial angles match with those of space groups I4/m of tetragonal phase (β-FeOOH: Akaganeite) and Pbnm of orthorhombic phase (α-FeOOH: Goethite), indicating the fact that the powder is composed of two different phases of FeOOH. However, β-FeOOH is the major constituent amounting to 98.07% while α-FeOOH contributes only 1.93% to the powder diffraction pattern. The interplanar spacing, *d*, presented in Table SI-4 shows a decrease as compared to the standard sample reported in ICSD, indicating the fact that the lattice is strained. Therefore, Williamson-Hall (W-H) method was used to measure the micro-strain and the crystallite size by plotting $\beta\cos\theta$ *vs.* $4\sin\theta$ of the relation reported elsewhere [48,49]. W-H plots for the β- and α-FeOOH are presented in **Fig. SI-2 (b)** and **(c)**, respectively, and the pertinent crystallite size and micro-strain data are given in Table SI-2, showing crystallite size of 53 nm and 25 nm, respectively, for the β- and α-FeOOH phases. As shown by the W-H plots in **Fig. 2 (b)** and **(c)** of the β- and α-FeOOH phases, respectively, the micro-strain (slope) has positive and negative values, indicating that the strain is tensile in case of β-FeOOH phase and compressive in case of α-FeOOH phase [50,51]. Rietveld refined XRD pattern (labelled as FO80-P$_{(ac)}$) of the post-calcination powder retrieved from autoclave which was processed at 80°C is presented in **Fig. SI-3(a)**. The refined XRD pattern shows that the film is composed of a single phase *i.e.*, cubic Fe_3O_4 in Fd-3m space group. The calculated lattice constants are slightly shorter than the standard reported in PDF [01-076-1849]. The effect is also observed on the interplanar spacings which are also slightly shorter than those of the standard. The average particle size and micro-strain were obtained from W-H plot which is presented in **Fig. SI-3 (b)**. The linear fit gives a straight line which is not perfect. Therefore, indicating that there is some dispersion in size and micro-strain of the film particles. The average crystallite size determined from W-H plot is ~37.23 nm (Table SI-2). The micro-strain of 0.0012 (0.12%) is positive, indicating that the micro-strain of the particles is due to lattice expansion. Rietveld refined XRD patterns of the pre- and post-calcination, and carbon-coated films on Cu substrate retrieved from autoclave after hydrothermal processing at 80°C are presented in SI along with their pertinent data. Rietveld refined XRD pattern of the as prepared film (labelled as FO80-0) is presented in **Fig. SI-4(a)**, which matches exactly with a single phase *i.e.*, α-FeOOH (space group: Pbnm), indicating that the film is composed of only one phase contrary to the residual powder which were mainly composed of β-FeOOH. Furthermore, the lattice constants and the interplanar spacing of the α-FeOOH constituting the film are significantly increased as compared to α-FeOOH of powder and the standard (Table SI-2 and 4). The W-H plot in **Fig. SI-4(b)** shows higher linearity which indicates that the film particles are homogeneous compared to the particles of residual powder. The crystallite size of 153.83 nm was estimated from the W-H plot. A positive micro-strain of 0.0024 (0.24%) indicates that the film particles are under tensile strain. Rietveld refined XRD pattern (**Fig. SI-5**) of the calcined film (labelled as FO80-1) matches with standard XRD pattern of cubic Fe_3O_4 having space group Fd-3m. The lattice constants of FO80-1 are smaller compared to that of powder sample and the standard XRD pattern of Fe_3O_4 given by PDF [01-076-1849]. Therefore, it is pertinent to confirm that the calcined film (FO80-1) is Fe_3O_4 and not maghemite (γ-Fe_2O_3), as the two have nearly indistinguishable crystal structures with the main difference being their lattice constants, which are smaller (~8.34 Å) for γ-Fe_2O_3 and relatively larger (~8.39 Å) for Fe_3O_4, whereas we observed ~8.363 Å for FO80-1, which lies somewhere in between the two. Previously, it has been reported that γ-Fe_2O_3 gives two additional small peaks at 2θ of 23.77° and 26.10° [52], which we did not observe in the diffractograms of FO80-1. Additionally, Kim *et al.* [52] comprehensively investigated the Fe_3O_4 and γ-Fe_2O_3 systems, and proposed a method involving the comparison of reflection from (511) plane, which gives a doublet if a mixture of the two phases is present. As shown in **Fig. SI-5(c)**, we could not observed a doublet for this very plane, instead a Voigt-fitted single peak around ~57.1° is given, corresponding to Fe_3O_4 phase [52]. It is pertinent to mention here that the reflection from (511) plane in case of γ-Fe_2O_3 phase emerges at 2θ >57.3° [52]. Furthermore, Schwaminger *et al.* [53] differentiated between the two phases using Raman spectroscopy, which showed peaks at ~660 cm^{-1} for the Fe_3O_4 and 710 cm^{-1} for the γ-Fe_2O_3 [53]. Here in case of FO80-1, the Raman spectrum (**Fig. SI-14(b)**) gives a single peak at 651 cm^{-1}. Even upon deconvolution, the γ-Fe_2O_3 peak reported at 710 cm^{-1} is not observed (**Fig. SI-14(h)**). The decrease in lattice constant of FO80-1 as compared to that of the standard Fe_3O_4 could be corresponded to the lattice strain and distortions which are responsible for contraction of the unit cell as reported previously [54], and evident from the W-H plot in **Fig. SI-5(b)**, which shows compressive strain. Furthermore, the W-H plot (**Fig. SI-5(b)**) is completely straight and linear, indicating that the crystallites and/or particles and the micro-strain are homogeneously distributed. The crystallite size estimated from W-H plot is ~14.66 nm and the micro-strain -0.0007 (0.07%). XRD pattern of the thermal CVD carbon coated film (FO80-2) was subjected to Rietveld refinement and found that the basic composition of the film remain unchanged as it matches exactly with the Fd-3m space group of Fe_3O_4 (**Fig. SI-6(a)**). The measured lattice constants and the interplanar spacings are in good agreement with those of the standard, but larger than those of the precursor. The W-H plot in **Fig. SI-6(b)** shows some deviation from the straight line, indicating that the homogeneous distribution of particle and micro-strain are somewhat disturbed. The estimated particle size from W-H plot is 28.85 nm which is almost double the particle size of its precursor film. Although the micro-strain has a negative value (-0.0006) as of the precursor, but increased slightly. Rietveld refined XRD pattern of MP-CVD carbon coated film (FO80-3) is presented in **Fig. SI-7(a)**, showing that the film is composed of two phases *i.e.*, Fe_3O_4 (space group Fd-3m) and pure iron (Fe) which crystallizes in space group Im-3m. The lattice constants of Fe_3O_4 have been increased slightly compared to its precursor but remained smaller than that of standard given by PDF [01-076-1849]. Likewise, the lattice constants of cubic Fe are slightly smaller than that of standard Fe in PDF [01-087-0721]. The percent fraction of Fe in the film is less than 1%. The crystallite size from W-H plot, in case of Fe_3O_4 phase, and Scherrer's equation, in case of Fe, were estimated, respectively, 22.35 nm and 24.00 nm. The W-H plot in **Fig. SI-7(b)** of Fe_3O_4 phase is exactly straight indicating that the particles and micro-strains are homogeneously

View Article Online
DOI: 10.1039/D6YA00012F

distributed. The negative value of micro-strain shows a compressive strain in the particles amounting to -0.0005 (0.05%). The negative and smaller value of micro-strain further indicates that the peaks broadening are insignificantly affected by micro-strain.

Rietveld refined XRD pattern of sample (FO120-P$_{(bc)}$) received as powder from autoclave, which was processed at 120°C, is presented in **Fig. SI-8(a)**. The powder is composed of two phases *i.e.*, Fe_3O_4 in space group Fd-3m and $FeCO_3$ in space group R-3c. The percent fraction of the two phases are, respectively, 91.95% and 08.05%, indicating that the main phase is cubic Fe_3O_4. The interplanar spacings of Fe_3O_4 phase lattice are increased slightly compared to that of standard lattice in PDF [01-076-1849]. However, there is observed a significant deviation from standard in lattice constants of $FeCO_3$ phase. The W-H plots of the two phases *i.e.*, Fe_3O_4 and $FeCO_3$ are presented, respectively, in **Fig. SI-8(b)** and **(c)**, showing a marked difference between them. As evident from the straight line, the particles of Fe_3O_4 are more homogeneously distributed than the particles of $FeCO_3$. Furthermore, the crystallites of the two phases are differently strained as evident from the positive slope (tensile strain) of Fe_3O_4 and negative slope (compressive strain) of $FeCO_3$ W-H plots. The crystallite size estimated from W-H plots are 72.05 nm (Fe_3O_4) and 50.28 nm ($FeCO_3$). The post-calcination powder sample (FO120-P$_{(ac)}$) was Rietveld refined and found that the resulting material consists of a single phase *i.e.*, cubic Fe_3O_4 (space group: Fd-3m), as shown by the Rietveld refined XRD pattern in **Fig. SI-9(a)**. From the Tables SI-5 and SI-7, it is evident that there is no significant change in lattice parameters upon calcination of the as received powder from autoclave at 120°C. However, the crystallite size estimated from W-H plot in **Fig. SI-9(b)** is significantly large *i.e.*, ~114.03 nm compared to 72.05 nm of its precursor. Rietveld refined XRD pattern of the pre-calcination film (FO120-0) achieved by hydrothermal processing at 120°C (**Fig. SI-10(a)**) shows that the film is also composed of two phases alike the residual powder. However, the percent fractions of the two phases *i.e.*, Fe_3O_4 and $FeCO_3$ in the film are quite different than those in residual powder. Contrary to the 8.05% share of $FeCO_3$ in composition of the powder, the film is composed of 35.17% of $FeCO_3$. The particles are under tensile strain and more homogeneously distributed as evident, respectively, from the positive slope (micro-strain) and straight lines of W-H plots of Fe_3O_4 and $FeCO_3$ given in **Fig. SI-10 (b)** and **(c)**. The crystallite size estimated are 33.22 (Fe_3O_4) nm and 42.85 nm ($FeCO_3$). From the Tables SI-5 and SI-7, it is evident that the lattice parameters deviates slightly from those of standard lattices. The post-calcination Rietveld refined XRD pattern of film (FO120-1) given in **Fig. SI-11(a)** shows a single phase *i.e.*, cubic Fe_3O_4 (space group: Fd-3m). The lattice constants of cubic Fe_3O_4 phase decreased significantly compared to the lattice constants of the same phase in its precursor. However, the crystallite size determined from W-H plot in **Fig. SI-11(b)** increased up to 46.42 nm. Furthermore, contrary to the precursor, the W-H plot deviates significantly from straight line and gives negative slope, indicating that the particles are less homogeneously distributed and under compressive strain. The post-calcination film upon coating with carbon by T-CVD (FO120-2) was subjected to Rietveld refinement and found that the refined XRD pattern matches very well with the cubic Fe_3O_4 (space group: Fd-3m) as shown in **Fig. SI-12(a)**. No significant change in its lattice parameters was observed compared to the those of the precursor but the crystallites size is witnessed to be decreased to 37.91 nm from 46.42 nm of its precursor. This may be owed to the so-called pore-wedge effect. Contrary to the FO80-2, FO120-2 involves the evolution of CO_2 which is responsible for creation of larger pores in the skeleton. During carbon coating by T-CVD, the C_2H_2 precursor molecules easily diffuse deep into these internal pores. The following carbon deposition then exert compressive strain through mechanical pressure, which leads to the fragmentation of the Fe_3O_4 crystallites and thus decrease in their size [55]. The W-H plot in **Fig. SI-12(b)**, which gives a negative plot and increased deviation from straight line, further support this explanation. Rietveld refined XRD pattern of film (FO120-3) obtained by coating the calcined film with MP-CVD is presented in **Fig. SI-13(a)**, showing that the film is composed of two phases *i.e.*, cubic Fe_3O_4 (space group: Fd-3m) and cubic Fe (space group: Im-3m) in percent fraction of 93.73% and 6.27%, respectively. The W-H plot in **Fig. SI-13(b)** for the cubic Fe_3O_4 phase is positive and shows lesser deviation from straight line compared to its precursor. This indicates that the Fe_3O_4 particles have tensile stress and more homogeneous distribution. Furthermore, the crystallite size (58.63 nm) of Fe_3O_4 phase is far larger than of its precursor (46.42 nm) and the T-CVD coated film (37.91 nm).

The films were characterized by Ramen spectroscopy to get some insight into the nature of the film materials. The as synthesized film (FO80-0) by hydrothermal processing at 80°C showed almost identical Raman spectrum as was reported previously [56,57]. As shown in **Fig. SI-14(a)**, the peaks are quite broad and thus overlapped, but their positions are corresponding to those of α-FeOOH (Goethite) [56,57]. Upon calcination of FO80-0, the Raman spectrum given in **Fig. SI-14(b)** of film FO80-1 shows a peculiar peak of cubic Fe_3O_4 (magnetite) at 651 cm^{-1} for the A_{1g} mode [58–60]. Besides, we can see another strong peak at 1306 cm^{-1}, which is corresponded to the decomposition of Fe_3O_4 to Fe_2O_3 upon irradiation of the sample with strong laser light during Raman measurements [61]. Raman spectrum in **Fig. SI-14(c)** is presented for the sample (FO80-2) obtained by coating the post-calcination film (FO80-1) with T-CVD. As one can see that the Raman spectrum shows a peculiar peak for the magnetite (cubic Fe_3O_4) at 669 cm^{-1} as was observed in the Raman spectrum of its precursor. Besides the magnetite peaks, the Raman spectrum of the film (FO80-2) shows two other distinct peaks at 1347 cm^{-1} and 1581 cm^{-1}. These peaks are corresponded to the disordered (D-band) and graphitic (G-band) bands, respectively, of carbon [62]. These very bands were deconvoluted by fitting with Lorentzian function as shown in **Fig. 2(a)**, and found that the areas under D band is quite larger than the area under G band, indicating the fact that the carbon material is largely disordered. The ratio (I_D/I_G) of D and G bands was determined from the peaks area and found to be ~1.21. The same precursor film when coated by MP-CVD, the resulting film (FO80-3) gives Raman peaks for Fe_3O_4 and also for the carbon materials as shown in **Fig. SI-14(d)** and **Fig. 2(b)**. However, the carbon peaks are superimposed by the dominant peaks of Fe_3O_4 in contrary to that of T-CVD carbon coated film (FO80-2). The peak in the region of 850 cm^{-1} to 1950 cm^{-1} were deconvoluted to extract the peaks of the carbon materials. As shown in **Fig. 2(b)**, the peak of D-band is weaker than the overlapped peaks of the Fe_2O_3, which come from decomposition of Fe_3O_4 under the Raman laser light, while that of G-band is further weaker [62]. The ratio of I_D/I_G is ~1.72, which is larger than that of T-CVD coated Fe_2O_4 film (FO80-2). This indicates that the disordered

View Article Online
DOI: 10.1039/D6YA00012F

carbon is larger in quantity as compared to the ordered carbon [62]. As we would see in the following sections, the lower intensity of the carbon peaks in presence of magnetite peaks could also be due to the thinner carbon coating around magnetite particles as compared to carbon coating produced by T-CVD. The post calcination sample (FO120-1) which was obtained from the precursor film processed hydrothermally at 120°C shows in its Raman spectrum in **Fig. SI-14 (e)** a peculiar peak of cubic Fe_3O_4 (magnetite) at 665 cm^{-1}. However, this very film upon coating with carbon by T-CVD shows in its Raman spectrum in **Fig. SI-14(f)** peaks besides those of magnetite (cubic Fe_3O_4). The peaks at 1315 cm^{-1} and 1565 cm^{-1} are the corresponding peaks of D- and G-band of carbon material. The two peaks were deconvoluted using the Lorentzian function and the ratio of I_D/I_G was determined to be ~2.11, as shown in **Fig. 2(c)**. Raman spectrum in **Fig. SI-14(g)** for the samples FO120-3 (film obtained by carbon coating with MP-CVD of the post-calcination film obtained at 120°C by hydrothermal processing) gives the peculiar peaks of magnetite (cubic Fe_3O_4). Besides, peaks for carbon material appears at 1323 cm^{-1} and 1538 cm^{-1} due to the D- and G-band, respectively. Although the peak for D-band is quite clear, but the G-band peak could only be obtained through deconvolution of the spectrum employing Lorentzian function. As presented in **Fig. 2(d)**, the deconvoluted spectrum gives peaks for D- and G-band with a ratio of 2.13, indicating the fact that the carbon material is for the most part a disordered one [62].

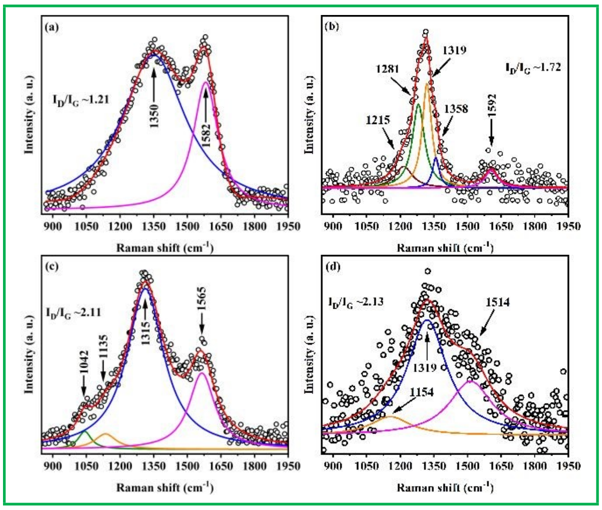

Fig. 2. (a) Deconvoluted Raman spectra of sample FO80-2 (a), FO80-3 (b), FO120-2 (c) and FO120-3 (d) in the region of 850 cm^{-1} to 1950 cm^{-1}, showing the D- and G-band of the carbon material

XPS was used to probe the elemental compositions and valence states of the surfaces of pre- and post-calcination, and carbon coated post-calcination films. The as prepared, by hydrothermal processing at 80°C, film (FO80-0) shows a typical α-FeOOH (Goethite) XPS survey spectrum (**Fig. SI-15(a)**) with major peaks of Fe 2p, O 1s and Fe 3p, corresponding very well to the reported XPS spectra of α-FeOOH [63,64]. As shown in **Fig. SI-15(a)**, the XPS spectrum of FO80-0 also shows peaks of carbon (C 1s) and Fluorine (F 1s), which could be corresponded to the presence of adsorbed organic species from solvents and NH_4F, respectively. As shown in **Fig. 3(a)**, Fe 2p bands appear at binding energy (BE) of 711.0 eV and 724.9 eV for the $2p_{3/2}$ and $2p_{1/2}$, respectively [65]. Besides, two peaks at 719.7 eV and 732.4 eV appear, respectively, for the satellite peaks of Fe $2p_{3/2}$ and Fe $2p_{1/2}$ [63,66–68]. Each of the Fe 2p peaks shows two sub-bands upon deconvolution at 710.7 eV and 712.8 eV, and 724.7 eV and 727.8 eV, respectively, for the Fe $2p_{2/3}$ and Fe $2p_{1/2}$ bands, indicating 3+ (*i.e.*, Fe^{3+}) valence state of Fe. Materials having Fe in its Fe^{3+} valence state show this sort of typical bands for Fe 2p [65,69,70]. The O 1s spectrum of sample FO80-0 is given in **Fig. 3(b)**, showing BE peaks at 529.8 eV, 531.2 eV, 532.2 eV and 533.4 eV, respectively, for the lattice oxygen (Fe-O), lattice hydroxyl group (Fe-OH), adsorbed hydroxyl group (Fe-OH_{ads}) and adsorbed water (H_2O) [71,72]. The deconvoluted O 1s spectrum shown in **Fig. 3(b)** reveals that the contribution of lattice Fe-O and lattice Fe-OH are predominant. The presence of Fe-OH_{ads} could be justified by the fact that the water (H_2O) after adsorption on Fe species decomposes to OH when subjected to heating. The film were prepared by processing the Fe-based material at elevated temperature (80°C) in a tightly closed vessel (*i.e.*, autoclave). Therefore, the adsorbed water would have been transformed upon the surface of α-FeOOH film according to the following chemical reaction (Eq. 3), which was previously proposed based on the temperature programmed desorption (TPD) studies [72].

$$H_2O \rightarrow OH_{ads} + H_{ads} \qquad (3)$$

Owing to this reaction on Fe, the contribution of Fe-OH_{ads} is increased than the contribution of adsorbed H_2O [72]. XPS survey spectrum of post-calcination film (FO80-1) is presented in **Fig. SI-15(b)**. By comparing it with its precursor's XPS survey spectrum, one can clearly see that the peaks of F are completely vanished, while the peaks of carbon decreased in intensity to be nearly insignificant. From these observations it is obvious that the F and C peaks in its precursor's XPS spectrum were owed to the presence of adsorbed F and carbon species, which upon calcination were removed. The significant peaks shown in XPS spectrum of FO80-1 are owed to Fe 2p, O 1s and Fe 3P. Fe 2p spectrum is presented in **Fig. 3(c)**, showing two peaks of Fe $2p_{3/2}$ and Fe $2p_{1/2}$ at 710.8 eV and 724.5 eV, respectively, resembling the reported Fe 2p spectrum of Fe_3O_4 [73]. The ratio of $2p_{3/2}/2p_{1/2}$ determined from the area under the peaks is approximately 1.65, which is closer to the expected value of 2. The Fe $2p_{3/2}$ and Fe $2p_{1/2}$ peaks were deconvoluted and found the peaks for Fe^{2+} at 710.4 eV and 724.1 eV, and Fe^{3+} at 712.7 eV and 727.0 eV, which are in good agreement with the previously reported values of pure Fe_3O_4 [74]. The Fe $2p_{3/2}$ satellite peak shifts to lower value on one hand, and on the other hand is poorly resolved owing to the overlapping of satellite structures of the octahedral Fe^{2+} and Fe^{3+}, a characteristic of Fe_3O_4 [74]. The ratio of Fe $2p_{3/2}$ satellite peak over the main Fe $2p_{3/2}$ is quite small *i.e.*, 0.09 (8.5% of the main peak), which is reaching above 0.45 in case of iron oxide containing only Fe^{3+} (like γ-Fe_2O_3 and α-Fe_2O_3) [74]. This indicates that the post-calcination film is primarily composed of Fe_3O_4. The O 1s spectrum in **Fig. 3(d)** shows an increased contribution of the lattice oxygen (*i.e.*, Fe-O) as compared to its precursor. This is further indication of the fact that the precursor α-FeOOH transformed to Fe_3O_4 upon calcination under the applied heat treatment regime. The contribution from adsorbed H_2O is insignificant (ratio of main Fe-O to H_2O peak is ~0.04 compared to 0.10 in case of precursor). Similarly, the ratio of main Fe-O peak to OH_{ads} is lowered to 0.19 from 0.49 of the precursor. On the other hand, the ratio of main Fe-O peak to Fe-OH increased by ~293%, confirming further that the main phase of the post-calcination film is

View Article Online
DOI: 10.1039/D6YA00012F

Fe_3O_4. This is in good agreement with the XRD and Raman data presented above. The full survey spectrum of the carbon coated post-calcination film (FO80-2) is presented in **Fig. SI-15(c)**, showing peaks for the core shell electrons of Fe 2p, O 1s and C 1s besides the peaks for Fe 3p and Fe 3s. Contrary to the XPS spectrum of its precursor, the core level electrons peak of C 1s is quite strong and prominent, indicating the fact that the film is coated with the required element *i.e.*, carbon. The deconvoluted Fe 2p spectrum of FO80-2 is presented in **Fig. 3(e)**, showing a BE peak at 711.1 eV and another one at 724.5 eV for the core electrons of Fe $2p_{3/2}$ and Fe $2p_{1/2}$, respectively [75]. The peaks were deconvoluted to 710.2 eV and 712.4 eV (Fe $2p_{3/2}$), and 724.1 eV and 728.2 eV (Fe $2p_{1/2}$). The Fe^{2+} to Fe^{3+} ratio was calculated to be 0.37:0.63, which slightly deviates from the 0.33:0.67 ratio of stoichiometric Fe_3O_4 expressed as $FeO \cdot Fe_2O_3$ [75]. This indicates the fact that the resulting film contains nearly stoichiometric Fe_3O_4, corresponding the XRD and Raman data presented above. Furthermore, the single phase of iron oxide *i.e.*, Fe_3O_4 composing the film is evident from two others but important features of the Fe 2p spectrum. One, the satellite peak at 719.1 eV which is trademark of pure Fe^{3+} based materials is completely absent in the XPS spectrum of Fe 2p of the film FO80-2. Second, the shoulder peak at 710.2 eV which appears for Fe^{2+} in the Fe_3O_4 became quite prominent as compared to its precursor [74]. From these observation it is quite clear that by treating the film in T-CVD, we did not only incorporate the carbon coating around the Fe_3O_4 but also improved the crystallinity of the iron oxide to single phase Fe_3O_4. The O 1s spectrum of FO80-2 in **Fig. 3(f)** shows a dominant peak at 530.5 eV for the lattice oxygen (Fe-O). There are two other important peaks in O 1s spectrum of FO80-2 film, appearing at BE of 531.7 eV and 532.9 eV which are corresponded to the core shell electrons of carbon involved in bonding with oxygen of Fe_3O_4 in Fe-O-C and C-O bonds, respectively [28–30]. It is worth mentioning here that the formation of Fe-O-C bond indicates a strong interaction between the core (*i.e.*, Fe_3O_4) and the shell (*i.e.*, carbon). This interaction is particularly important for enhanced strength of encapsulation of core in shell, improving the conductivity by shedding of Fe_3O_4 from carbon matrix on one hand. On the other hand, it helps in stabilizing the Fe_3O_4 by restraining its particles aggregations during electrochemical applications [76]. A peak appearing at 534.0 eV in the O 1s spectrum of FO80-2 shows an insignificant contribution to this very spectrum from the adsorbed water species. It is possible that the insignificant amount of water has been adsorbed during handling of the sample. The high resolution core level XPS spectrum of C 1s is presented in **Fig. 3(g)**, showing a main peak at 284.8 eV which is corresponded to the graphitized carbon (sp^2-C) [77–81]. This indicates that most of the carbon atoms are in conjugated hexagonal form [80]. The peak at 286.0 eV is corresponded to the C-O, indicating that the carbon shell is strongly bonded with the Fe_3O_4 core through Fe-O-C bonding as was also observed in XPS spectrum of O 1s [77–79]. The tail of the peak at higher BE side was also deconvoluted to small peaks appearing at 287.4 eV and 288.9 eV which correspond to C=O and O-C=O [77,78,80–82]. The deconvoluted peak at 290.7 eV is corresponded to the π-π* of the graphitic carbon [82]. Alike the FO80-2 film, XPS spectrum in **Fig. SI-15(d)** of carbon coated Fe_3O_4 by MP-CVD shows three main peaks for the core electrons of Fe 2P, O 1s and C 1s. The high resolution XPS spectrum of Fe 2p is presented in **Fig. 3(h)**, showing the usual two peaks of Fe $2p_{3/2}$ and Fe $2p_{1/2}$ at 710.7 eV and 724.2 eV, respectively. These very peaks were deconvoluted to 710.1 eV (Fe^{2+}) and 712.2 eV (Fe^{3+}), and 723.9 eV (Fe^{2+}) and 727.8 eV (Fe^{3+}). The satellite peak at 719.4 eV is negligible, indicating that the material is single phase pure Fe_3O_4. The O 1s spectrum of FO80-3 shows three peaks at 530.5 eV, 531.8 eV and 532.9 eV corresponding to lattice oxygen (Fe-O), oxygen bridging iron and carbon (Fe-O-C) and C-O, respectively [78–80]. Unlike its precursor and the T-CVD carbon coated Fe_3O_4 film (FO80-2), the high resolution C 1s spectrum of MP-CVD coated Fe_3O_4 film (FO80-3) shows only three peaks at 284.7 eV, 286.2 eV and 288.24 eV, corresponding to C-C, C-O and C=O, respectively, of the graphitic carbon, most probably of graphene [82,83].

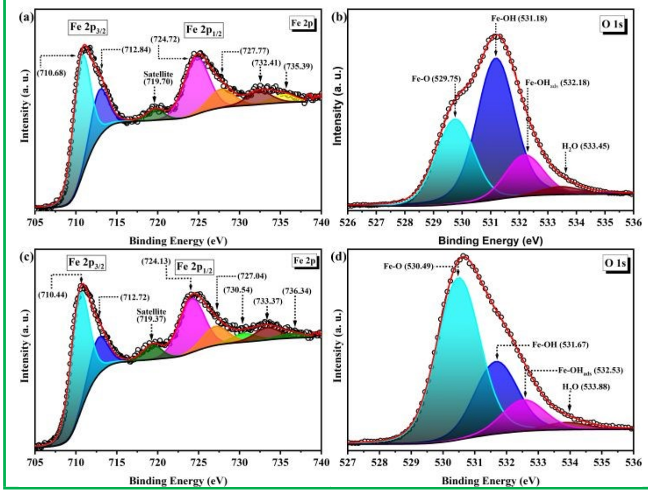

View Article Online
DOI: 10.1039/D6YA00012F

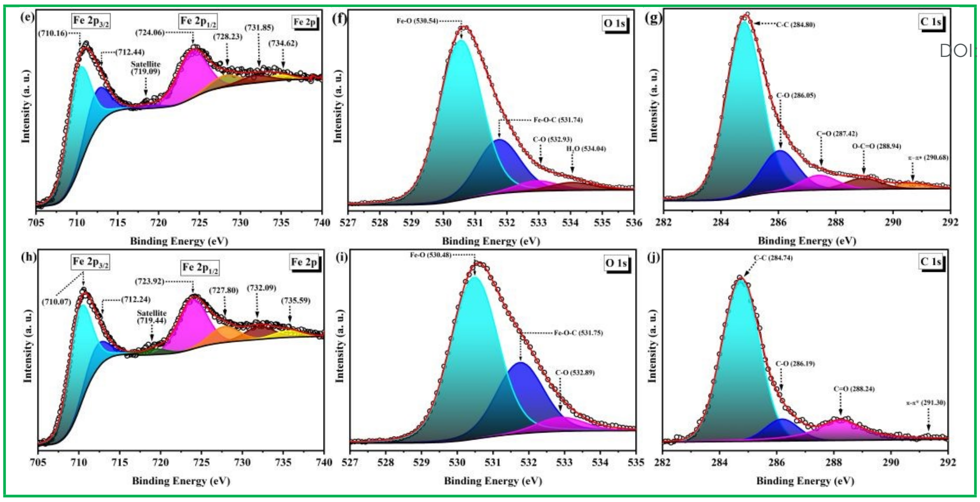

Fig. 3. XPS spectra of (a) Fe 2p and (b) O 1s of FO80-0, (c) Fe 2p and (d) O 1s of FO80-1, (e) Fe 2p, (f) O 1s and (g) C 1s of FO80-2, and (h) Fe 2p, (i) O 1s and (j) C 1s of FO80-3

The films prepared at 120°C by hydrothermal technique and followed by heat treatment to get the calcined film (FO120-1) which was then coated with carbon by T-CVD (FO120-2) and MP-CVD (FO120-3) were also studied by XPS analysis to get their elemental compositions and valence states. The relevant XPS survey spectrum of the post-calcination film (FO120-1) is presented in **SI-15(e)** which shows core electron peaks of Fe 2p and O 1s along an insignificant peak of C 1s, corresponding to the XPS spectrum of post-calcination film (FO80-1). The high resolution Fe 2p XPS spectrum of FO120-1 is presented in **Fig. 4(a)** which shows two peaks at 711.0 eV and 724.6 eV for the Fe $2p_{3/2}$ and Fe $2p_{1/2}$, respectively. Both the peaks were deconvoluted to get the contribution from Fe^{2+} and Fe^{3+} to each peak. The Fe $2p_{3/2}$ gives deconvoluted peaks at 710.4 eV and 712.6 eV for the contribution of Fe^{2+} and Fe^{3+}, respectively. Likewise the Fe $2p_{1/2}$ peak is deconvoluted to two peaks at 724.3 eV and 728.9 eV, respectively, for the contribution of Fe^{2+} and Fe^{3+}. These values correspond to post-calcination film (FO80-1) and the reported Fe_3O_4 materials, indicating that the film is composed of cubic Fe_3O_4 as revealed by XRD and Raman data presented in the preceding sections. Furthermore, as was shown by the post calcination film FO80-1, Fe 2p XPS spectrum of the post calcination film FO120-1 also shows a clear shoulder at around 710.1 eV and flattened satellite peak at 719.3 eV which is obviously insignificant. The appearance of clear shoulder and absence of satellite peak is peculiarity of Fe_3O_4 [74]. This indicates the fact that the film in FO120-1 is composed of single phase Fe_3O_4. Contrary to the as retrieved films, the deconvoluted O 1s core electron XPS spectrum presented in **Fig. 4(b)** of FO120-1 shows main peak at 530.7 eV, corresponding to the lattice oxygen *i.e.*, Fe-O. Like the post calcination film FO80-1, O 1s XPS spectrum of FO120-1 also shows peaks at 531.6 eV, 532.6 eV and 533.8 eV for the Fe-OH, $Fe\text{-}OH_{ads}$ and H_2O oxygen, respectively. The adsorbed water contribution to the O 1s spectrum is nearly negligible, and could be due to the adsorbed water during handling of the sample. XPS survey spectra of the post calcination film coated with carbon by T-CVD (FO120-2) and MP-CVD (FO120-3) are presented in **Fig. SI-15(f)** and **(g)**, respectively, showing peaks for the elements Fe, O and C. The high resolution Fe 2p XPS spectrum presented in **Fig. 4(c)** and **(f)** are almost identical, and correspond to those of FO80-2 and FO80-3. This indicates the fact that the films are composed of Fe_3O_4 for its iron contents. The high resolution O 1s XPS spectra presented in **Fig. (d)** and **(g)**, respectively, of FO120-2 and FO120-3 are in good agreement too with the high resolution O 1s spectra of FO80-2 and FO80-3. As shown in the XPS survey spectra (**Fig. SI-15**), the T-CVD and MP-CVD carbon coated films *i.e.*, FO120-2 and FO120-3, respectively, show C 1s core electrons peak which is nearly negligible in their precursor film *i.e.*, FO120-1. Furthermore, the high resolution C 1s XPS spectra of FO120-2 and FO120-3 presented, respectively, in **Fig. 4(e)** and **(h)** are no different than the C 1s spectra of FO80-2 and FO80-3. This indicates that the Fe_3O_4 material of FO120-2 and FO120-3 films is successfully encapsulated in carbon materials.

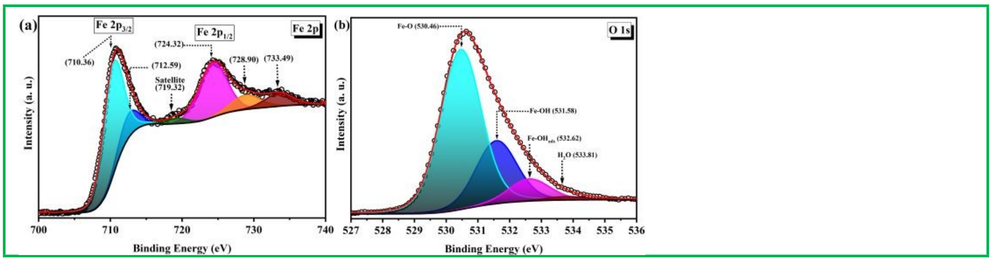

View Article Online
DOI: 10.1039/D6YA00012F

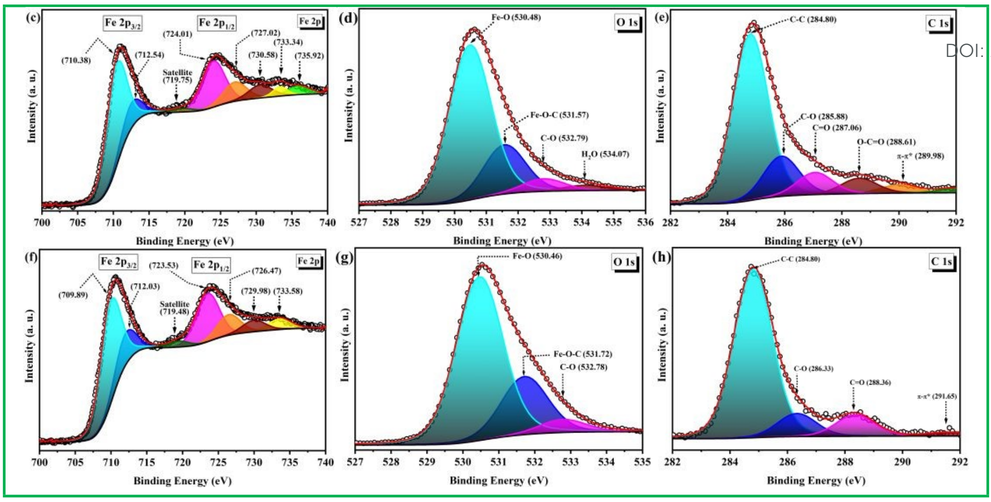

Fig. 4. XPS spectra of (a) Fe 2p and (b) O 1s of FO120-1, (c) Fe 2p, (d) O 1s and (e) C 1s of FO80-2, (f) Fe 2p, (g) O 1s and (h) C 1s of FO80-3

Structural morphology of the film surfaces were examined by FE-SEM and the pertinent FE-SEM images are presented in **Fig. 5** and **Fig. SI-16**. As shown in FE-SEM image in **Fig. SI-16(a)**, the as synthesized film (FO80-0) by hydrothermal processing at 80°C gives densely populated nanorods (NRs) which are uniformly grown on the Cu substrate surface. The high resolution FE-SEM image of FO80-0 in **Fig. SI-16(b)** shows that the NRs have rhombus shape, having sides of equal lengths and smooth surfaces. The average side length ranges between 205 nm to 400 nm, and an induced edge angle of 50° which is peculiarity of the rhombus shape. Previously, an identical morphology was reported for Co_3O_4 when it was realized under, nearly, the same synthesis conditions which were applied here by us [42,43]. Upon calcination, morphological structure of the film (FO80-1) does not varied significantly. As one can see in **Fig. 5(a)**, FE-SEM image of FO80-1 film shows densely populated Cu-substrate surface with NR arrays. The high magnification FE-SEM image of FO80-1 in **Fig. 5(b)** shows that the basic rhombus shape of the NR arrays is intact after calcination. It is evident from the FE-SEM images of samples FO80-2 and FO80-3 in **Fig. 5(c)** and **(e)**, respectively, that the morphological structure upon the Cu-substrate surfaces pronounced more than in their precursor (*i.e.*, FO80-0). However, in case of both the carbon coated samples *i.e.*, FO80-2 and FO80-3, the basic rhombus structure of the NR arrays remained intact, which is evident from their high magnification FE-SEM images given, respectively, in **Fig. 5(d)** and **(f)**. Although the basic rhombus structure was preserved upon carbon coatings, but the surface of the NR arrays becomes coarse in case of FO80-2, and coarse and porous in case of FO80-3. The T-CVD carbon coated rhombus NR arrays also shown an increase in length of their edges and a change in induced edges angles. The average edge length of the rhombus NRs are ranging between 325 nm and 475 nm while the induced edges angle between 45° and 63°. The significant increase in edge length and the change in edges angle could be corresponded to the carbon coating which may have brought some deformation to the basic structure of the rhombus NR arrays. Contrarily, the MP-CVD carbon coated rhombus NRs arrays show a slight increase in their edge lengths and angles, indicating that the carbon coating is thin and more uniform by MP-CVD than the T-CVD.

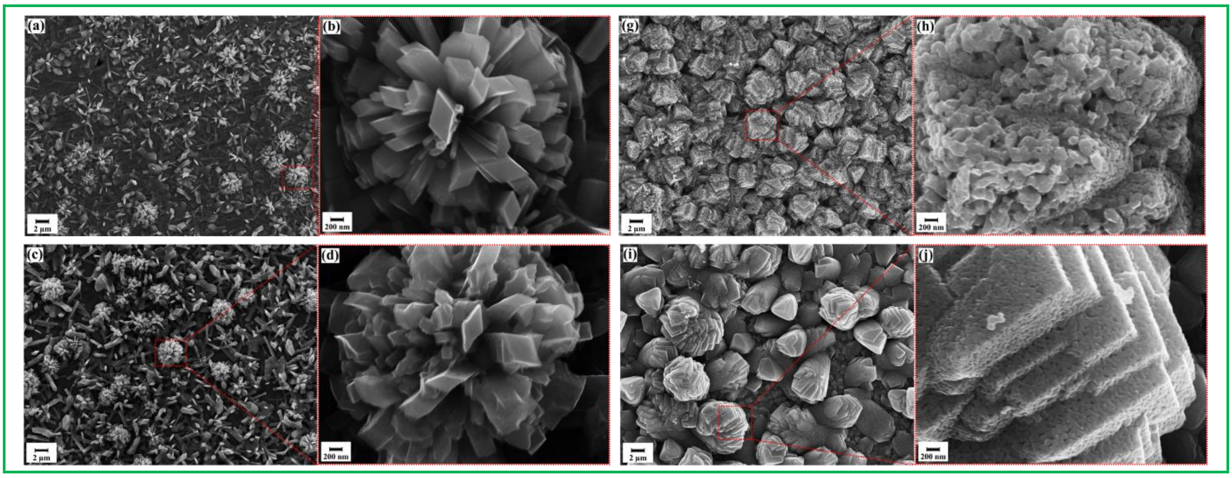

View Article Online
DOI: 10.1039/D5YA00012F

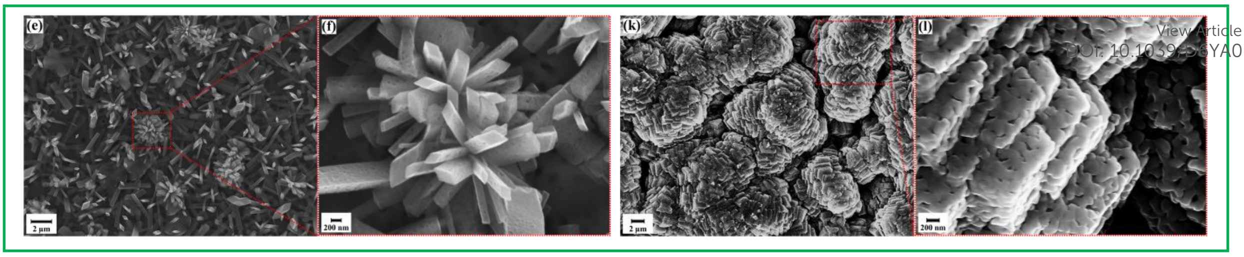

Fig. 5. Low as well as high magnification FE-SEM images of FO80-1 ((a) & (b)), FO80-2 ((c) & (d)), FO80-3 ((e) & (f)), FO120-1 ((g) & (h)), FO120-2 ((i) & (j)), and FO120-3 ((k) & (l))

Structural morphology of the as synthesized film (FO120-0) at 120°C for 12 hours is quite the same as reported earlier [26]. However, contrary to that, the morphology in this case is realized at higher hydrothermal temperature *i.e.*, at 120°C. As shown in **Fig. SI-16(c)**, FE-SEM image of the sample FO120-0 shows nanolayers which are assembled to give layer-by-layer three dimensional (3D) superstructures. The high magnification FE-SEM image of FO120-0 in **Fig. SI-16(d)** shows that the nanolayers are actually formed of the self-assembled nanoparticles. Upon calcination, the basic morphology is retained as shown by the FE-SEM image of FO120-1 in **Fig. 5(g)**. The high resolution FE-SEM image of the same film in **Fig. 5(h)** indicates very clearly the nanolayers which are formed of nanoparticles. The layered structure of the precursor is also preserved in the carbon coated films *i.e.*, FO120-2 and FO120-3 by T-CVD and MP-CVD, respectively. However, contrary to the precursor and also the post-calcination films, the carbon coated film show porous morphology. Using the EDX analyzer coupled with FE-SEM, elemental compositions of the films were also studied, and the pertinent data are presented in the **Fig. SI-17**. The EDX spectra and the corresponding elemental mappings show all the essential elements of the films. It is pertinent to mention here that the EDX spectra of the precursor films *i.e.*, FO80-0 and FO120-0 also show peaks for fluorine (F_2) besides the peaks for integral elements of the films.

TEM image of FO80-0 is given in **Fig. SI-18(a)**, showing self-assembled NR arrays, conforming to the morphology shown by FE-SEM images in **Fig. SI-16(a)** and **(b)**. The high magnification TEM image which is given as inset in **Fig. SI-18(a)** shows a single rod having length of 1.96 µm and width of 430 nm, indicating the fact that the NR arrays have length in micrometers while width in nanometers. Furthermore, the high magnification TEM image as inset in **Fig. SI-18(a)** shows that the NR are quite smooth, having no structures on their surfaces. The HR-TEM image of FO80-0 is presented in **Fig. SI-18(b)**, showing clear lattice fringes of ~0.273 nm which corresponds to the interplanar distance of 0.269 nm of lattice plane (130) of α-FeOOH [84]. Inset in **Fig. SI-18(b)** is given the Fast Fourier Transformed (FFT) pattern of the HR-TEM image. The clear pattern of dots shown by the FFT image indicate the fact that the NR arrays are crystalline in nature, conforming to the XRD results. Elemental composition of the NR arrays was also studied by EDX coupled with TEM. As shown in **Fig. SI-18(c)**, the EDX spectrum of FO80-0 shows peaks for the integral elements *i.e.*, Fe and O of α-FeOOH. Besides, peaks of C and F are also clearly shown as were shown in EDX spectrum obtained by EDX analyzer coupled with SEM. EDX line scan profile of a single NR was obtained along the line indicated in **Fig. SI-18(d)**, showing C pattern which is mainly owed to the carbon film of the TEM grid. It is pertinent to mention here that the carbon film supported TEM grids were used to provide support to the nanoparticles during TEM analysis. Elemental mapping images in **Fig. SI-18(e)** shows uniform distribution of the two essential elements *i.e.,* Fe and O besides of F. However, in the elemental mapping image of C, the background carbon film is more visible than any carbon of NR array. TEM image of the post-calcination film *i.e.*, FO80-1 is given in **Fig. SI-18(f)**, showing NR arrays having lengths and widths comparable to those of the precursor (FO80-0). The NRs have smooth surfaces as was the case with their precursor, showing no additional features and/or structures over their surfaces as is evident from the high magnification TEM image presented as inset in **Fig. SI-18(f)**. HR-TEM image presented in **Fig. SI-18(g)** shows clear fringes with spacings of 0.260 nm, 0.300 nm and 0.460 nm, respectively, corresponding to the interplanar spacings of lattice planes (311), (220) and (111) of cubic Fe_3O_4 [85]. This conforms the XRD data which shows that upon calcination, the α-FeOOH film completely transforms to Fe_3O_4 under the applied calcination regime. The crystalline nature of the film material of FO80-1 is further evident from FFT image presented as inset in **Fig. SI-18(g)**, showing a clear pattern of dots. EDX spectrum in **Fig. SI-18(h)** of FO80-1 shows only the essential elements *i.e.,* Fe and O of Fe_3O_4, and contrary to the precursor, F peak is missing in the EDX spectrum of post-calcination film as was the case with the EDX spectrum obtained by EDX analyzer coupled with SEM. However, C peak could be seen and could be owed to the carbon film of TEM grid. EDX line scan profile of a single NR was obtained along the line indicated in **Fig. SI-18(i)**. As shown by the graph in **Fig. SI-18(i)**, the Fe and O are uniformly distributed over the entire NR. The insignificant profile of C could be owed to the carbon film of TEM grid. This is further evident from the EDX mapping images of FO80-1 presented in **Fig. SI-18(j)**, showing uniform distribution of Fe and O over the entire NR. However, EDX mapping of C is clearly shown to be due to the carbon film of TEM grid.

Low magnification TEM images of the film, FO80-2, obtained after carbon coating of the post-calcination film (FO80-1) have shown NRs arrays having lengths in micrometers while diameter spanning over a large range, conforming its SEM images. Upon scratching from the substrate and then dispersing in ethanol for casting on the TEM grid, the smaller width NR arrays mostly remained agglomerated as shown in **Fig. SI-19(a)** while the larger width NR arrays dispersed completely into individual NR as shown in **Fig. 6(a)**. Contrary the precursor, surfaces of the NR arrays turned rough upon carbon coating in T-CVD. The STEM HAADF images presented as inset in **Fig. 6(a)** and **Fig. SI-19(a)**, shows blind holes which seems to be formed by etching the surface by the reactive gas. The high magnification TEM images presented in **Fig. 6(b)** and **Fig. SI-19(b)** show a central-

View Article Online
DOI: 10.1039/D6YA00012F

part (core) covered by a thin shell. The FFT performed over the central-part (*i.e.,* core) shows a clear pattern of dots while the overlayer (shell) shows no diffraction spots, as given in insets of **Fig. 6(b)** and **Fig. SI-19(b)**. This indicates the fact that the character of the core is crystalline while that of shell is amorphous. HR-TEM images of NR arrays are presented in **Fig. 6(c)** and **Fig. SI-19(c)**, showing well defined fringes at ~0.498 nm and 0.300 nm for the interplanar spacings of lattice planes (111) and (220) , respectively, of cubic Fe_3O_4 [85]. EDX spectra measured over an agglomerate as well as standing alone NRs show peaks for the three elements *i.e.*, Fe, O and C as shown in **Fig. SI-19(d)**. As indicated in **Fig. SI-19(e)**, the EDX line scan profile of a single NR shows variation in Fe, O and C distribution. While passing through the ends and the surface holes of NR array, intensity of C line surges while those of Fe and O decrease, indicating the fact that the C surrounds the Fe_3O_4 particles. This fact is further evident from the EDX elemental mapping images in **Fig. 6(d)** and **Fig. SI-19(f)**, showing although uniform distribution of the elements Fe, O and C, but the C intensity is stronger at the extremities and at the holes in the NR array. To discern the increased intensities at the extremities and the holes in the NR arrays, the scratched film was subjected to strong and prolonged ultrasonication and then drop cast over the TEM grid. TEM image given in **Fig. SI-19(g)** shows that the holes worked as fissure lines, supporting disintegration of the NR arrays into non-uniform core-shell particles. High magnification TEM image in **Fig. SI-19(h)** was subjected to FFT and found that the shell is amorphous as the FFT pattern is blurry while the core is crystalline as the FFT pattern shows clear pattern of dots. HR-TEM image in **Fig. SI-19(i)** shows that the core is primarily made up of Fe_3O_4 by giving clear fringes of 0.450 nm which correspond to the interplanar spacing of lattice plane (111) of cubic Fe_3O_4. MP-CVD carbon coated film (FO80-3) is no more different in its morphological structure than the T-CVD carbon coated film (FO80-2). The low and high magnification TEM images in **Fig. 6(e)** and **(f)**, respectively, show NR arrays having rough surface with holes as those of FO80-2. High magnification and HR-TEM images in **Fig. 6(f)** and **(g)**, respectively, show that the NR arrays are consisting of crystalline particles of Fe_3O_4 surrounded by amorphous carbon as depicted by the FFT dot patterns and fringes, and blurry FFT pattern, respectively. This is further supported by the EDX data and their line scan profile depicted in **Fig. SI-20(c)** and **(d)**, respectively. Contrary to the precursor (FO80-1) as well as the T-CVD coated film (FO80-2), the EDX line scan profile show decreased O intensity in comparison to the intensity of Fe. It is understandable as the MP-CVD carbon coated film contains metallic Fe besides Fe_3O_4, increasing overall contents of Fe in comparison to O. The presence of metallic Fe is well established from the powder XRD data presented in the preceding sections.

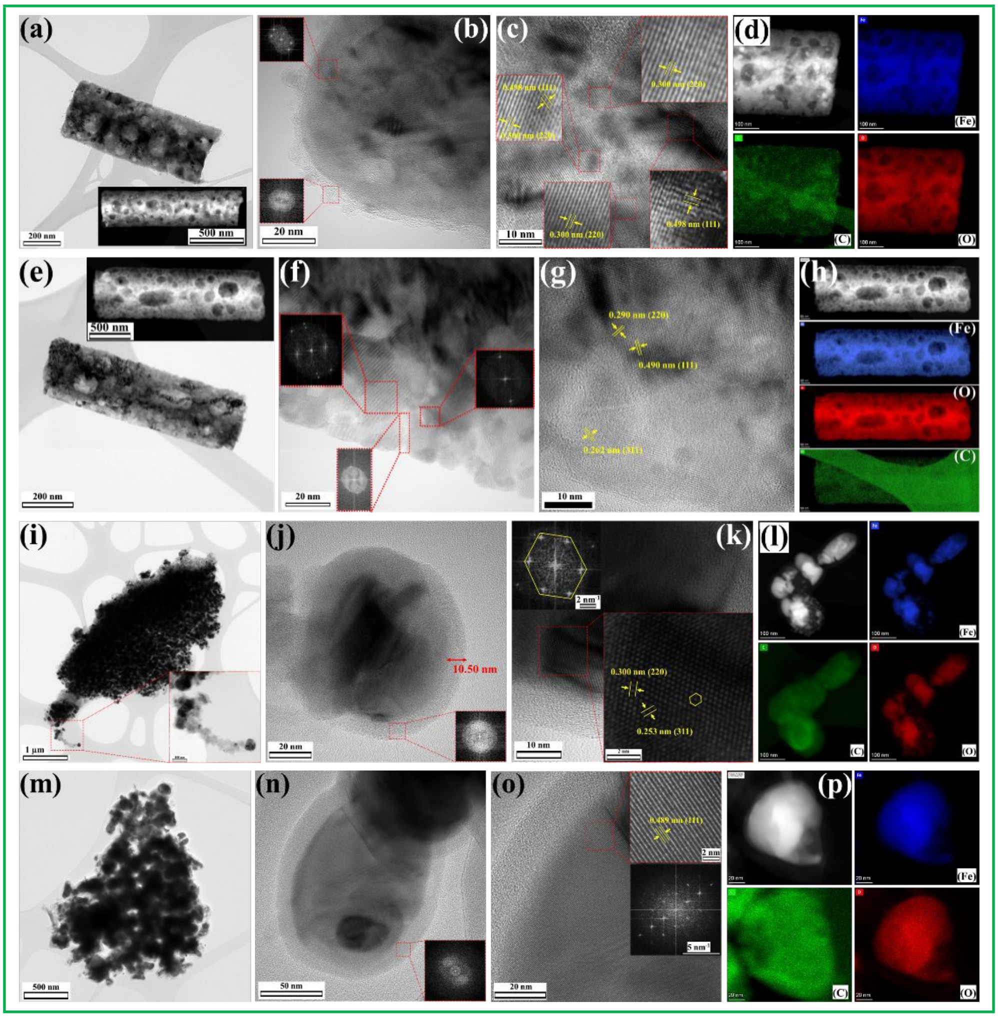

View Article Online
DOI: 10.1039/D6YA00012F

Fig. 6. Low (a) and high (b) magnification TEM images, HR-TEM image with FFT as inset (c), and elemental mapping (d) of FO80-2, low (e) and high (f) magnification TEM images, HR-TEM image with FFT as inset (g), and elemental mapping (h) of FO80-3, low (i) and high (j) magnification TEM images, HR-TEM image with FFT as inset (k), and elemental mapping (l) of FO120-2, low (m) and high (n) magnification TEM images, HR-TEM image with FFT as inset (o), and elemental mapping (p) of FO120-3

To get clear insight of material's morphology, T-CVD coated post-calcination film (FO120-2) obtained by hydrothermal processing at 120°C was subjected to prolonged ultrasonication before drop casting on the TEM grid. In **Fig. 6(i)** is presented TEM image which shows tiny particles arranged into a layer. High magnification TEM image in **Fig. 6(j)** shows that the particle are consisting of core (average size ~73 nm) and shell (average thickness ~9.5 nm). The shell is amorphous as is shown by the blurry FFT pattern presented as inset in **Fig. 6(j)**. The core on the other hand is crystalline and is supported by the very clear fringes of 0.300 nm and 0.253 nm corresponding to the interplanar spacings of lattice planes (220) and (311), respectively, of cubic Fe_3O_4 (**Fig. 6(k)**). Furthermore, crystallinity of the core is also evident from its FFT pattern comprising of clear dots as shown as inset in **Fig. 6(k)**. The core and shell structure of the particles is also evident from the elemental mapping images of Fe, O and C in **Fig. 6(l)**. EDX line scan profile along the line depicted in **Fig. SI-20(e)** shows a clear surge in carbon intensity at the extremities of the particles while at the center the Fe and O intensities are stronger. Morphology of MP-CVD carbon coated film material is no different than the T-CVD carbon coated film material, which is evident from the TEM, HR-TEM and elemental mapping images presented in **Fig. 6(m)** and **(n)**, **(o)** and **(p)**, respectively. However, EDX line scan profile along the line depicted in **Fig. SI-20 (f)** shows increased intensity of Fe in comparison to the O intensity exactly in the same fashion and for the same reason as was the case with MP-CVD carbon coated film FO80-3. Furthermore, the C intensity is increased at the extremities while it is almost uniform in the middle, indicating overlapping of the Fe_3O_4 particle by carbon shell.

Electrochemical behavior of the samples was studied by cyclic voltammetry (CV) and the pertinent data are presented in **Fig. 7**. The voltammograms were measured while applying cut-off potentials of -1.0 V and 0 V at different scan rates (*v*) ranging from 5 mVs^{-1} up to 150 mVs^{-1} in 1 molar Na_2SO_4 solution. Cyclic voltammograms of the as prepared Fe_3O_4 film (FO80-1) which was obtained by calcination of the as received film from hydrothermal processing at 80°C is presented in **Fig. SI-21(a)**, showing nearly identical voltammograms to the previously reported ones [86]. Besides that Fe_3O_4 is generally considered a negative electrode material of pseudocapacitive nature, the nearly symmetrical nature of the curves with redox peaks supports the fact that the film possesses pseudocapacitive properties. The broad redox peaks could be owed to the Fe^{II}/Fe^{III} redox reactions which may also be accompanied by the (de)intercalation of Na^+ ion to maintain the local charge neutrality [87,86]. The phenomenon which was also previously observed for Fe_3O_4 and other charge storage materials is depicted by the following chemical reaction (Eq. 4), where *x* is the mole fraction of Na^+ ion (de)intercalated [86,88–90].

$$Fe_3O_4 + xe^- + xNa^+ \rightarrow Na_xFe_3O_4 \qquad (4)$$

Furthermore, the current intensity increases with increasing *v* but the shape remains almost unchanged even up to *v* of 150 mVs^{-1}, indicating the fact that the Fe_3O_4 film has good rate capability with rapid redox reaction occurring on the electrode [91]. To understand the electrochemical kinetics of the Fe_3O_4 film, current at fix anodic and cathodic potentials of -0.243 V and -0.607 V, respectively, was plotted against the square root of varying *v*. As shown in **Fig. SI-21(b)**, the relationships between the current and the square root of *v* is deviating from linear, indicating that the redox reaction is pre-dominantly controlled by capacitive process [92]. To further understand the nature of the current, either capacitive or diffusion-controlled, CV data at various *v* were analyzed by following the power law (Eq. 5) [93].

$$i = av^b \qquad (5)$$

In this equation (Eq. 5), *i* is the current at a selected voltage V and *v* is the scan rate while *a* and *b* are adjustable parameters. The contribution of current, either capacitive or diffusion-controlled, depends upon the *b* value which is determined from the slope of log(*i*) *vs.* log(*v*) plot. When it is close to 1, the current is predominantly capacitive in nature while when it is close to 0.5 the current is predominantly diffusion-controlled [94]. The value of *b* determined from log(*i*) *vs.* log(*v*) plot given in **Fig. SI-21(c)** is equal to ~0.879, indicating that the contribution of current to the CV curve is predominantly from charge storage by capacitive process. Furthermore, the percentage contribution to the CV curve from capacitive and diffusion-controlled processes was determined following the equation (Eq. 6) [95,96].

$$i(V) = k_1v + k_2v^{1/2} \qquad (6)$$

where *i*(V) is current at given potential, and k_1v and $k_2v^{1/2}$ are the capacitive-controlled (I_c) and diffusion-controlled (I_d), respectively, current fractions contributing to the total stored current. The equation could be further simplified by rearranging to the one shown in (Eq. 7).

$$i(V)\Big/_{v^{1/2}} = k_1v^{1/2} + k_2 \qquad (7)$$

v, and k_1 and k_2 are the scan rate, and adjustable parameters, respectively, which can be determined from the slope and intercept of the plot between $i(V)/v^{1/2}$ and $v^{1/2}$ (**Fig. SI-21(d)**). The percentage capacitive and diffusion-controlled current contributions are presented in **Fig. SI-21(e)**, showing higher capacitive contributions as compared to the diffusion-controlled on one hand. On the other hand, it shows increasing capacitive current contribution with increasing scan rate, indicating the fact that the capacitive charge storage process is dominant in storing the total charge by the Fe_3O_4 film (FO80-1).

The post-calcination film after coating with carbon by T-CVD was also followed by CV for exploration of its electrochemical characteristics, and the pertinent CV curves at cut-off voltage range of -1.0 V to 0.0 V at varying *v* are presented in **Fig. 7(a)**. As depicted by the CV scans in **Fig. 7(a)**, the carbon-coated film (FO80-2) shows a higher charge storage than its precursor (FO80-1), which is evident from the comparison of areas under the closed patterns. Furthermore, it is also evident from the specific capacitance values, which increased significantly upon carbon coating of the film, as shown by the **Fig. SI-22(a)**. The increase in specific capacitance could be attributed to enhanced electrical conductivity on the one hand and, on the other hand, reduced charge-transfer resistance due to the carbon coating. Alike the precursor film (FO80-1), CV curves of FO80-2 (carbon-coated film) shows clear but remarkably enhanced redox peaks, indicating that the film has strong pseudocapacitive and/or diffusion-controlled capacity [97]. This corresponds to the vast literature citing Fe_3O_4 as negative electrode material of pseudocapacitive nature [97]. The increase in strength of current-potential response giving wider CV curves of FO80-2 film as compared to its precursor FO80-1 film could be corresponded to the carbon coating, which increases the conductivity on one hand, and on the other hand, contributing to charge storage through its own electrochemical double layer (EDL) process [98]. Furthermore, the multiple redox peaks appearing in the CV curves of FO80-2 are corresponded to the fact that the film underwent a number of valence state transformation under the applied potential window. The plots in **Fig. 7(b)** of peak current (i_p) of the prominent oxidation and reduction peaks as a function of the square root of v shows a linear relationship, indicating that the charge storage is dominated by diffusion-controlled process. The anodic and cathodic i_p - (*scan rate*) plots were linear fitted and the measured correlation coefficient (R^2) values of 98.2% and 98.7%, respectively, indicate that film shows battery behavior while storing charge dominantly by diffusion-controlled process [99]. **Fig. 7(c)** of the prominent anodic and cathodic peaks also shows a linear relationship, giving slopes (= b values according to Eq. 5) of 0.695 and 0.681, respectively. This further support the fact that diffusion-controlled process is the dominant mechanism for charge storage. As shown in **Fig. 7(d)**, the percentage contribution of diffusion-controlled process towards the total charge storage is higher in case of carbon-coated film (FO80-2) than its precursor film (FO80-1). Even at 100 mV/s, the percent contribution from diffusion controlled process is half of the total charge storage as shown in **Fig. 7(e)**. The enhanced contribution of charge storage by diffusion controlled process could be corresponded to the carbon coating as well as to the morphology of the film. The conductive carbon coating provide highways for rapid and efficient transport of electron and ions, thus supporting the diffusion controlled charge storage process [100]. Additionally, as one can see in the TEM and SEM images presented in the preceding sections, the particles of carbon-coated films possess large number of tiny holes compared to the particles of precursor which have smooth surfaces. This holes could allow the electrolyte to reach deep into the bulk of the film particles, ensuring pseudocapacitive process on the surface as well as in the bulk. In fact nano porous structures facilities rapid diffusion of electrons and ions, thus enhancing the share of charge storage by diffusion controlled process [101]. This is further evident from the EIS Nyquist plot presented in **Fig. SI-22(a)**, showing a small semi-circle at the higher frequency end while a strong and steeper oblique line at an angle of approximately 45°. The semicircle represents the resistance to the charge transfer at interface, while the oblique line is the Warburg resistance, a resistance to the diffusion of ions [102]. This indicates that mostly the charge transfer occurs through diffusion-controlled process, and thus the contribution of diffusion-controlled charge storage is higher than the capacitive. The post-calcination film (FO80-1) upon coating with carbon by MP-CVD shows, in principle, an identical CV curves in the potential window of -1.0 V to 0.0 V at varying v as depicted in **Fig. 7(f)**. The enclosed area under CV curves is larger than its precursor (FO80-1) and smaller than T-CVD carbon coated film (FO80-2). The electrochemical charge storage mechanism is dominated by the pseudocapacitive process which is evident from the peaks in its CV scans. It is further supported by the linear relationship of i_p-$(v)^{1/2}$ curves presented in **Fig. 7(g)**, giving R^2 values close to 1 for the anodic and cathodic peaks. Following Eq. 5, b values were determined by plotting log(i_p) versus log(v) as shown in **Fig. 7(h)**. It is also evident from the b values that the charge storage mechanism is dominated by diffusion-controlled process. The percentage charge storage contribution either capacitive or diffusion-controlled to the total was determined by following the Eq. 7. As presented in **Fig. 7(i)**, the charge storage mechanism at lower scan rates is dominated by diffusion-controlled amounting to approximately 62% at 5 mV/s, decreasing with increasing scan rate. As shown in **Fig. 7(j)**, diffusion controlled charge storage share in case of FO80-3 (MP-CVD carbon coated Fe_3O_4 film) drops to ~26% as compared to that of T-CVD coated Fe_3O_4 film (~46%) but still higher by ~19% compared to that of the FO80-1 (bare Fe_3O_4 film). These observations signify the impact of carbon coating and the nano porosity upon the charge storage mechanism.

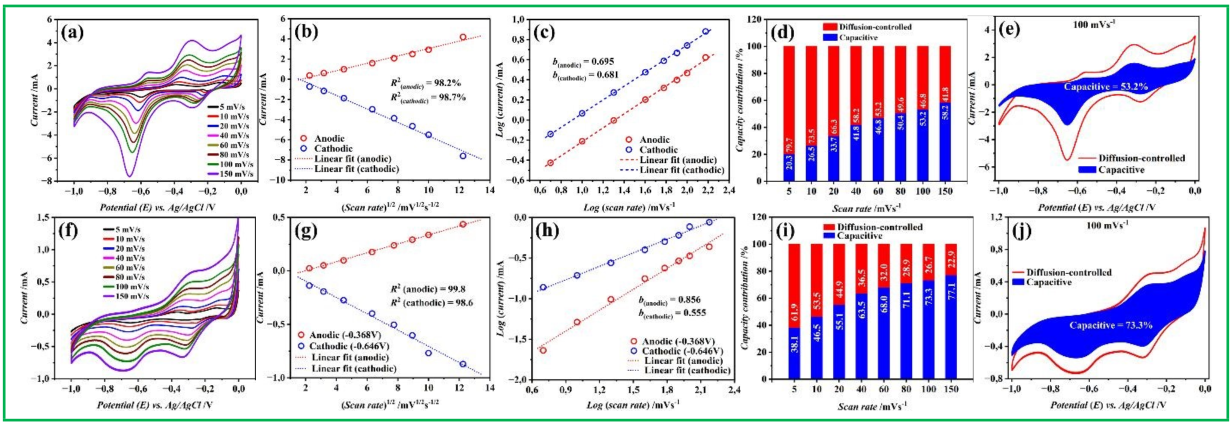

Fig. 7. CV curves of FO80-2 (a) and FO80-3 (f) at varying v of 5 mV/s to150 mV/s in 1M Na_2SO_4 in the potential range of 1.0 V to 0.0 V, peaks current (i_p) *vs.* square root of scan rate ($v^{1/2}$) of FO80-2 (b) and FO80-3 (g), log(i) *vs.* log(v) plots for determination of b values of FO80-2 (c)

View Article Online
DOI: 10.1039/D6YA00012F

and FO80-3 (h), contribution proportions of diffusion-controlled and capacitive to the total charge storage at different scan rates of FO80-2 (d) and FO80-3 (i), and separation of diffusion-controlled and capacitive current at 100 mV/s of FO80-2 (e) and FO80-3 (j)

The CV curves of FO120-1 (the calcined film derived from the film prepared by hydrothermal processing at 120°C) are presented **Fig. SI-23(a)**, showing nearly rectangular shapes with an oxidation peak which increases in intensity with increasing scan rate of up to 40 mV/s. Afterwards, this very peak decreases in intensity and finally adopts a rectangular shape at 100 mV/s. this very peak also shifts towards right with increasing scan rate indicating an irreversible oxidation of the iron specie [103]. Contrary to the uncoated Fe_3O_4 film (FO120-1), the carbon coated, either by T-CVD or MP-CVD, films show nearly rectangular shapes of their CV curves, corresponding to the typical CV curves of carbon coated Fe_3O_4 materials reported earlier [101,104,105]. The R^2 and *b* values obtained from the graphs of *i* vs. *(v)*$^{1/2}$ and log(*i*) vs. log(*v*), respectively, lie in the range (see **Fig. 8(b)** and **(c)**) and **(g)** and **(h)**), respectively for the FO120-2 and FO120-3, which support major contribution from diffusion-controlled process to the total charge. The contribution proportions based on Eq. 7 at different scan rates in **Fig. 8(d)** and **(i)**, respectively, for the films FO120-2 and FO120-3 shows that the diffusion-controlled process is dominant at lower scan rates. Even at 100 mV/s, the contribution from diffusion-controlled process is almost half of the total charge stored.

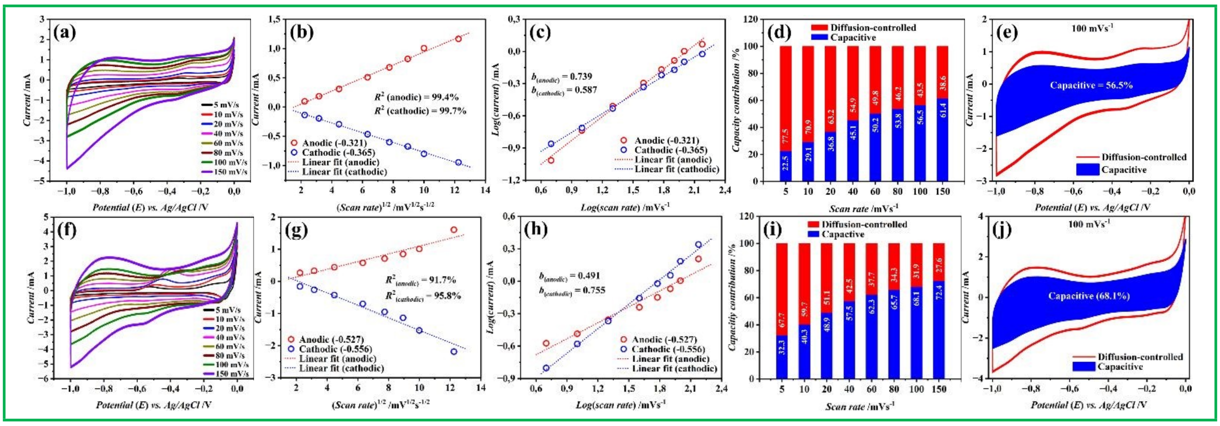

Fig. 8. CV curves of FO120-2 (a) and FO120-3 (f) at varying *v* of 5 mV/s to150 mV/s in 1M Na_2SO_4 in the potential range of 1.0 V to 0.0 V, peaks current (i_p) *vs.* square root of scan rate ($v^{1/2}$) of FO120-2 (b) and FO120-3 (g), log(*i*) *vs.* log(v) plots for determination of *b* values of FO120-2 (c) and FO120-3 (h), contribution proportions of diffusion-controlled and capacitive to the total charge storage at different scan rates of FO120-2 (d) and FO120-3 (i), and separation of diffusion-controlled and capacitive current at 100 mV/s of FO120-2 (e) and FO120-3 (j)

Based on the presented results, the deposition of films have been depicted by an illustration given in **Fig. 9**. As reported elsewhere [106], and observed here by us, the phase and morphological evolution of the films was found to be highly sensitive to the hydrothermal environment, which includes the autoclave pressure, hydrolysis kinetics of urea and substrate-directed nucleation. The urea undergoes competitive reactions, *i.e.,* oxidative hydrolysis and carbonation, depending on the hydrothermal process temperature. These reactions are given by the chemical equations (Eq. 8-10) in the following [107,108].

$$CO(NH_2)_2 + H_2O \xrightarrow{\Delta} 2NH_3 + CO_2 \qquad (8)$$

$$NH_3 + H_2O \rightarrow NH_4^+ + OH^- \qquad (9)$$

$$CO_2 + H_2O \rightarrow H_2CO_3 \rightarrow HCO_3^- + H^+ \rightarrow CO_3^{2-} + H^+ \qquad (10)$$

As evident from these equations, urea have served as pH-regulating agent at both the temperatures *i.e.,* 80°C and 120°C by releasing hydroxyl (OH^-) and carbonate (CO_3^{2-}) ions. In addition to these ions, the possible formation of transient metal fluoride complexes such as ($[FeF_n]^{(2-n)}$) may have moderated the process by preventing the premature precipitation [42]. Mostly derived from ionization of urea, all these ions have served as precursors for realization of either FeOOH (80°C) or $FeCO_3$ (120°C)after reacting with the iron ions (Fe^{2+}) under the applied hydrothermal processing conditions. Initially, the Fe^{2+} ions partially oxidized to $Fe(OH)_3$ during the solution formation at ambient (Eq. 11) [26].

$$Fe^{2+} + O_2 + H_2O \rightarrow Fe(OH)_3 \qquad (11)$$

The $Fe(OH)_3$ has strong potential for anchoring, and thus adhered to the surface of the copper (Cu) substrate, serving as seeds for nucleation process [42]. As the hydrothermal processing at 80°C proceeded, reaction occurred between the leftover Fe^{2+} ions and OH^- ions, which were produced during urea hydrolysis, giving FeOOH (Eq. 12). Furthermore, the $Fe(OH)_3$ produced in the previous step get converted to FeOOH (Eq. 13) [26].

$$4Fe^{2+} + 8OH^- + O_2 \rightarrow 4FeOOH + 2H_2O \qquad (12)$$

$$Fe(OH)_3 \rightarrow FeOOH + H_2O \qquad (13)$$

On the other hand, at the hydrothermal processing at 120°C, besides the formation of $Fe(OH)_3$ and FeOOH, precipitation of $Fe(CO_3)$ also occurred. It is pertinent to mention here that the formation of metal carbonates in hydrothermal processing at higher temperatures in presence of urea is not without a precedence [44,107,108].

View Article Online
DOI: 10.1039/D6YA00012F

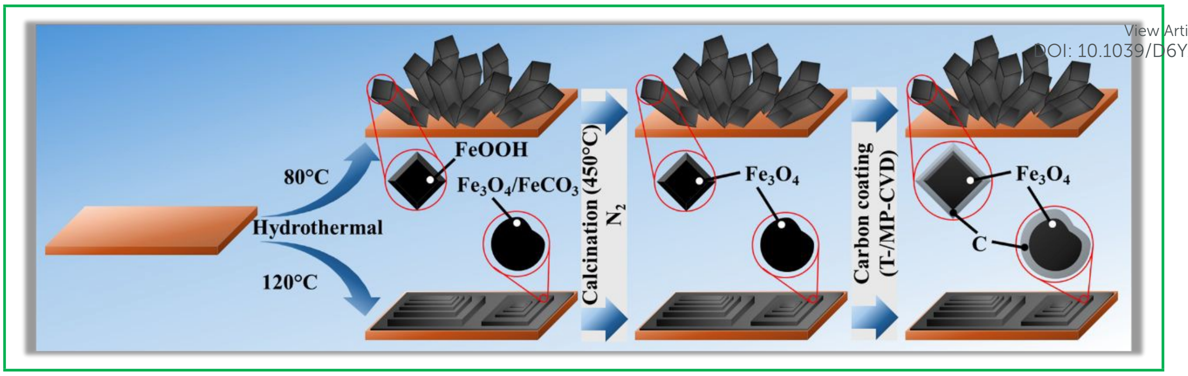

Fig. 9. Illustration of the process for preparation of resulting films

An interesting situation was observed at hydrothermal processing at 80°C. At this temperature, predominantly was observed the formation of α-FeOOH and β-FeOOH, respectively, at the substrate and in the bulk solution as a result of oxidative hydrolysis of Fe^{2+} ions (Eq. 12). This indicates that the Cu foil surface *i.e.,* the substrate surface supported the growth of α-FeOOH phase, while a suitable environment was provided by the solution for the growth of β-FeOOH phase. This is attributed to the difference in nucleation energies at the two different places *i.e.,* at the surface of substrate (Cu foil) and in the solution. The heterogeneous surface provided by Cu substrate stabilizes the thermodynamically favoured α-FeOOH phase (Goethite) through the potential lattice matching with the copper oxide surface layer which is inevitably formed during hydrothermal processing [109]. In fact, the preferential growth of the α-FeOOH phase on the substrate is owed to the lower interfacial energy provided by the Cu substrate surface [109]. On the other hand, the solution contains F^- ions furnished by the NH_4F precursor. These ions incorporate into the β-FeOOH phase (Akaganeite), which has a tunnel-type structure, and thus stabilize it. Therefore, owing to the availability of high local concentration of F^- ions in solution for formation of tunnel structures of FeOOH, the powder have dominant β-FeOOH phase [110]. It is pertinent to mention here that the achievement of single phase film *i.e.,* α-FeOOH is contrary to the mix phases *i.e.,* α-FeOOH/β-FeOOH reported by Cao *et al.* [26], while the experimental conditions were exactly the same except the autoclave size. Besides, there is a marked difference in morphology of the films. Instead of 3D framework of layered nanosheets of Cao *et al.* [26], we obtained 1D rhombus-shaped nanorods. The difference in morphology is owed then to the autoclave size as all other hydrothermal processing parameters were the same.

Rhombohedrons were commonly achieved owing to the oriented attachment growth [111]. It was observed that the realization of rhombohedrons at the expense of other structures through dissolution-reprecipitation process enhances with increasing amount of ammonia (NH_3). By using a larger vessel for the same amount of solution, the filling ratio (*f*) of the autoclave decreased from 70% in case of Cao *et al.* [26] to 56% in the present work, leading to creation of lower internal pressure [112]. The reduced internal pressure then facilitated and accelerated the urea hydrolysis reaction (Eq. 8) [113], producing increased amount of NH_3, which then ultimately favoured the formation of anisotropic 1D rhombohedral structures. It is also pertinent to mention here that the role of F^- as structure directing agent could not be ignored, as previously it was reported that F^- is critical in realization of 1D rhombus nanorods upon diverse substrate at hydrothermal temperatures below 100°C [42–44,114].

By increasing the temperature from 80°C to 120°C, the conditions resembling that of Cao *et al.* [26] may have been achieved even with the larger size autoclave, leading to the formation of the 3D framework of layered nanosheets. However, the increase in hydrothermal processing temperature also shifted the thermodynamic stability. As a result a phase transition occurred from oxyhydroxides at 80°C to a mixture of Fe_3O_4 and $FeCO_3$ at 120°C [44]. In fact, urea hydrolysis was further accelerated by the increasing hydrothermal temperature from 80°C to 120°C which increased then the concentration of CO_3^{2-} (Eq. 10), shifting the equilibrium toward the precipitation of $FeCO_3$ (Eq. 14) [108].

$$Fe^{2+} + CO_3^{2-} \rightarrow FeCO_3 \qquad (14)$$

Interestingly, the film contains significantly higher $FeCO_3$ content (~35%) than the precipitated powder (~8%). This highlights the role of Cu substrate in stabilizing the $FeCO_3$ nucleation under the applied hydrothermal conditions. Nonetheless, Fe_3O_4 is the dominant component in film as well as in the precipitate. This is due to the reaction between FeOOH and $Fe(OH)_2$ suspension under decreasing concentration of CO_3^{2-} [108].

$$2FeOOH + Fe(OH)_2 \rightarrow Fe_3O_4 + H_2O \qquad (15)$$

From this observations, the role of hydrothermal temperature upon the phase and the morphology of the nanostructures is obviously demonstrated.

Upon calcination at 450°C, all the as synthesized precursors underwent a topotactic transformation to Fe_3O_4. The fundamental morphologies *i.e.,* the rhombus-shaped 1D nanorods and 3D framework of layered nanosheets, respectively, from the 80°C and 120°C synthesis were preserved. This indicates the robustness of the nanostructures. However, tiny holes appears upon calcination at 450°C due to the decomposition and degassing of the volatile species [26]. These species are in fact the chemically bound water and CO_2 molecules, which evolve as a result of the decomposition of FeOOH and $FeCO_3$, respectively, upon heating.

As no reduction was induced by T-CVD, the Fe_3O_4 films were partially reduced to metallic iron (Fe) during carbon coating by MP-CVD. This was inevitable as the strong hydrogen plasma alongside the carbon precursor produces a more aggressive reducing environment [115]. Despite the reduction induced by the MP-CVD, the structural framework of the Fe_3O_4 nanostructures was robust enough to preserve the basic morphology. The preservation of morphology and

View Article Online
DOI: 10.1039/D5YA00012F

tiny holes during the carbon coating by T- and MP-CVD is critical for performance point of view. They maximize the surface area, ensuring high electrolyte accessibility in electrochemical applications. Effect of these factors have been clearly demonstrated by the synthesized films during their electrochemical characterization.

Conclusion

In conclusion, it is stated that carbon encapsulated Fe_3O_4 films as binder-free electrodes for potential application in energy storage devices were prepared directly on the Cu current collector by a scalable approach, involving hydrothermal growth in first step, followed by calcination in the second step and finally carbon coating by CVD in the third step. The results showed that the hydrothermal parameter *i.e.,* temperature has a marked influence on the phase and morphology of the films. It was found that the hydrothermal processing of the desired reactants at 80°C gives rhombus-shaped α-FeOOH nanostructures. At higher hydrothermal processing temperature of 120°C, the phase and morphology of the films were entirely different *i.e.,* nanolayers of $Fe_3O_4/FeCO_3$ composite arranged into 3D superstructures. The nanostructures were stable and robust enough that the basic morphology was retained after calcination and even after carbon coating by CVD techniques. Although the morphology was not affected by either the calcination or carbon coating, but the crystallographic phase changed from FeOOH to the desired phase *i.e.,* Fe_3O_4. Both the CVD techniques *i.e.,* T- and MP-CVD gave well-defined Fe_3O_4@C core-shell nanoarchitectures having strong interfacial interactions through the formation of Fe-O-C bridges. The crystallinity was further improved by MP-CVD, which also induced partial reduction of Fe_3O_4 to Fe. The electrochemical characterizations of the samples showed that the charge storage predominantly occurs by diffusion-controlled process at lower scan rates, while by capacitive process at higher scan rates. In addition to the improved charge storage, it was found that the charge transfer resistance is lower for the carbon-encapsulated binder-free electrodes. Furthermore, these electrodes have shown superior stability. The improvements in electrochemical characteristics were attributed to the synergistic benefits of Cu substrate which provided direct electron pathways, nanostructuration which shortened the diffusion pathlengths, and the carbon shells which provided a conductive protection. In nutshell it is concluded that the key limitation of Fe_3O_4 electrodes were addressed through a thoroughly explored strategy which include the control over film morphology, binder-free architecting, and carbon encapsulation. Therefore, we confidently say that the strategy offers a promising platform for realization of high rate and long-life anodes for next generation electrochemical energy storage devices, which include but not limited to batteries, supercapacitors and hybrid devices. Additionally, the rationally designed and viably realized strategy will pave the way for fabrication of metal-oxide-based electrodes which have improved performance on one hand, and on the other hand, potential of scalability.

Author contributions

All the authors contributed to the development of the manuscript. H. Ullah and S. Mortazavi conducted the experiments and investigated the processes. H. Ullah, S. Mortazavi, and A. M. Flatae acquired the data using various techniques. They also analysed the data. H. Ullah prepared the initial draft of the manuscript. A. M. Khan, X. Jiang and all the above mentioned authors contributed to the reviewing, editing and approving of the manuscript for publication.

Conflicts of interest

“There are no conflicts to declare”.

Data availability

All the data supporting findings of this manuscript are included in the manuscript and the associated ESI files.

Acknowledgements

H. Ullah acknowledges the financial support received to him from the European Union's Horizon 2020 research and innovation programme under the Marie Skłodowska-Curie grant agreement No. 945422. The authors greatly acknowledge “Gerätezentrum für Mikro- und Nanoanalytik MNaF, Siegen University, Germany” for providing support for the analysis of samples by FE-SEM, TEM, XRD, XPS *etc*.

References

1 N. Khan, S. Dilshad, R. Khalid, A. R. Kalair and N. Abas, *Energy Storage*, 2019, **1**, e49.

2 G. Smdani, M. R. Islam, A. N. Ahmad Yahaya and S. I. Bin Safie, *Energy Environ.*, 2023, **34**, 1094–1141.

3 J. Lu, Z. Chen, F. Pan, Y. Cui and K. Amine, *Electrochem. Energy Rev.*, 2018, **1**, 35–53.

4 J. B. Goodenough and K.-S. Park, *J. Am. Chem. Soc.*, 2013, **135**, 1167–1176.

5 M. Li, J. Lu, Z. Chen and K. Amine, *Adv. Mater.*, 2018, **30**, 1800561.

6 L. Zhao, B. Ding, X.-Y. Qin, Z. Wang, W. Lv, Y.-B. He, Q.-H. Yang and F. Kang, *Adv. Mater.*, 2022, **34**, 2106704.

7 N. Nitta, F. Wu, J. T. Lee and G. Yushin, *Mater. Today*, 2015, **18**, 252–264.

8 V. Patil, A. Patil, S.-J. Yoon and J.-W. Choi, *Sci. Adv. Mater.*, 2018, **10**, 507–512.

9 M. V. Reddy, G. V. Subba Rao and B. V. R. Chowdari, *Chem. Rev.*, 2013, **113**, 5364–5457.

10 M. M. Rahman, U. Nisar, A. Abouimrane, I. Belharouak and R. Amin, *Electrochem. Energy Rev.*, 2025, **8**, 14.

11 J. Zhu, Y. Ding, Z. Ma, W. Tang, X. Chen and Y. Lu, *J. Electron. Mater.*, 2022, **51**, 3391–3417.

12 C. Zhao, S. Yao, C. Li, Y. An, S. Zhao, X. Sun, K. Wang, X. Zhang and Y. Ma, *Chem. Eng. J.*, 2024, **497**, 154535.

13 H. Ren, H. Li, P. Barry, Z. Wang, A. R. Campos, E. S. Takeuchi, A. C. Marschilok, S. Yan, K. J. Takeuchi and E. Reichmanis, *Chem. Mater.*, 2024, **36**, 9299–9319.

View Article Online
DOI: 10.1039/D6YA00012F

14 J. Guan, Y. Chen, L. Cao, Y. Liu, P. Lian, Y. Gao and X. Shi, *J. Power Sources*, 2020, **469**, 228307.

15 N. Manikandan, B. Lakshmi and S. Shivakumara, *J. Solid State Electrochem.*, 2022, **26**, 887–895.

16 J. Ma, Y. Xu, Y. Xu, Y. Zhang, M. Zhang, Z. Cao and C. Liu, *J. Energy Storage*, 2025, **108**, 115164.

17 J. Tu, H. Tong, P. Wang, D. Wang, Y. Yang, X. Meng, L. Hu, H. Wang and Q. Chen, *Small*, 2023, **19**, 2301606.

18 J. P. Pender, G. Jha, D. H. Youn, J. M. Ziegler, I. Andoni, E. J. Choi, A. Heller, B. S. Dunn, P. S. Weiss, R. M. Penner and C. B. Mullins, *ACS Nano*, 2020, **14**, 1243–1295.

19 Z. Gao, S. Rao, J. Wang, D. Wang, T. Zhang, X. Feng, Y. Liu, J. Shi, Y. Xue, W. Li, L. Wang, C. Rong and Y. Chen, *ChemSusChem*, 2024, **17**, e202400830.

20 D. Deng, *Energy Sci. Eng.*, 2015, **3**, 385–418.

21 X. Chen, X. Zhu, G. Cao, S. Zhang, Y. Mu, H. Ming and J. Qiu, *Energy Fuels*, 2021, **35**, 1810–1819.

22 K. Shen, S. Zhai, S. Wang, Q. Ru, X. Hou, K. San Hui, K. Nam Hui and F. Chen, *Batter. Supercaps*, 2021, **4**, 860–880.

23 Y. Kang, C. Deng, Y. Chen, X. Liu, Z. Liang, T. Li, Q. Hu and Y. Zhao, *Nanoscale Res. Lett.*, 2020, **15**, 112.

24 O. Gerard, A. Numan, S. Krishnan, M. Khalid, R. Subramaniam and R. Kasi, *J. Energy Storage*, 2022, **50**, 104283.

25 Y. Yang, J. Li, D. Chen and J. Zhao, *ACS Appl. Mater. Interfaces*, 2016, **8**, 26730–26739.

26 K. Cao, L. Jiao, H. Liu, Y. Liu, Y. Wang, Z. Guo and H. Yuan, *Adv. Energy Mater.*, 2015, **5**, 1401421.

27 J. Chen, K. Huang and S. Liu, *Electrochimica Acta*, 2009, **55**, 1–5.

28 F. Bojabady, E. Kamali-Heidari and S. Sahebian, *Mater. Chem. Phys.*, 2023, **305**, 127828.

29 D. Q. Han, F. Yang, Y. Y. Gong and S. G. Yang, *Surf. Eng.*, 2015, **31**, 481–485.

30 C. He, S. Wu, N. Zhao, C. Shi, E. Liu and J. Li, *ACS Nano*, 2013, **7**, 4459–4469.

31 L. Wang, F. Liu, A. Pal, Y. Ning, Z. Wang, B. Zhao, R. Bradley and W. Wu, *Carbon*, 2021, **179**, 327–336.

32 J. Ryu, J. Park, W.-G. Lim and J. Hwang, *Appl. Surf. Sci.*, 2024, **675**, 160976.

33 Z. Liu, X.-Y. Yu and U. Paik, *Adv. Energy Mater.*, 2016, **6**, 1502318.

34 M. Li, H. Du, L. Kuai, K. Huang, Y. Xia and B. Geng, *Angew. Chem. Int. Ed.*, 2017, **56**, 12649–12653.

35 Z. Zeng, H. Zhao, J. Wang, P. Lv, T. Zhang and Q. Xia, *J. Power Sources*, 2014, **248**, 15–21.

36 E. Ngondo, X. Fuku, M. A. Kebede and N. W. Hlongwa, *ChemistrySelect*, 2025, **10**, e02667.

37 J. Wang, M. Gao, D. Wang, X. Li, Y. Dou, Y. Liu and H. Pan, *J. Power Sources*, 2015, **282**, 257–264.

38 B. Wang, G. Wang, Z. Zheng, H. Wang, J. Bai and J. Bai, *Electrochimica Acta*, 2013, **106**, 235–243.

39 A. T. Adeleye, K. I. John, P. G. Adeleye, A. A. Akande and O. O. Banjoko, *J. Mater. Sci.*, 2021, **56**, 18391–18416.

40 T. Sheng, Y.-F. Xu, Y.-X. Jiang, L. Huang, N. Tian, Z.-Y. Zhou, I. Broadwell and S.-G. Sun, *Acc. Chem. Res.*, 2016, **49**, 2569–2577.

41 S. E. F. Kleijn, S. C. S. Lai, M. T. M. Koper and P. R. Unwin, *Angew. Chem. Int. Ed.*, 2014, **53**, 3558–3586.

42 W. Mei, J. Huang, L. Zhu, Z. Ye, Y. Mai and J. Tu, *J. Mater. Chem.*, 2012, **22**, 9315–9321.

43 Z. Wen, L. Zhu, W. Mei, L. Hu, Y. Li, L. Sun, H. Cai and Z. Ye, *Sens. Actuators B Chem.*, 2013, **186**, 172–179.

44 Z. Wen, L. Zhu, W. Mei, Y. Li, L. Hu, L. Sun, W. Wan and Z. Ye, *J. Mater. Chem. A*, 2013, **1**, 7511–7518.

45 J. Rodríguez-Carvajal, *Phys. B Condens. Matter*, 1993, **192**, 55–69.

46 L. B. McCusker, R. B. Von Dreele, D. E. Cox, D. Louër and P. Scardi, *J. Appl. Crystallogr.*, 1999, **32**, 36–50.

47 A. Kumar and D. Varshney, *Ceram. Int.*, 2012, **38**, 3935–3942.

48 S. Debnath, K. Deb, B. Saha and R. Das, *J. Phys. Chem. Solids*, 2019, **134**, 105–114.

49 M. Kuru, T. Ş. Kuru, E. Karaca and S. Bağcı, *J. Alloys Compd.*, 2020, **836**, 155318.

50

51 N. S. Gonçalves, J. A. Carvalho, Z. M. Lima and J. M. Sasaki, *Mater. Lett.*, 2012, **72**, 36–38.

52 W. Kim, C.-Y. Suh, S.-W. Cho, K.-M. Roh, H. Kwon, K. Song and I.-J. Shon, *Talanta*, 2012, **94**, 348–352.

53 S. P. Schwaminger, C. Syhr and S. Berensmeier, *Crystals*, DOI:10.3390/cryst10030214.

54 A. Gholizadeh, *J. Am. Ceram. Soc.*, 2017, **100**, 3577–3588.

55 I. Lungu, T. Potlog, M. Dobromir and S. Moldovan, *ChemistrySelect*, 2026, **11**, e05915.

56 W. D. Chemelewski, H.-C. Lee, J.-F. Lin, A. J. Bard and C. B. Mullins, *J. Am. Chem. Soc.*, 2014, **136**, 2843–2850.

57 M. V. Abrashev, V. G. Ivanov, B. S. Stefanov, N. D. Todorov, J. Rosell and V. Skumryev, *J. Appl. Phys.*, 2020, **127**, 205108.

58 X. Wu, J. Tang, Y. Zhang and H. Wang, *Mater. Sci. Eng. B*, 2009, **157**, 81–86.

59 S. Tiwari, R. Prakash, R. J. Choudhary and D. M. Phase, *J. Phys. Appl. Phys.*, 2007, **40**, 4943.

60 C. Ruby, B. Humbert and J. Fusy, *Surf. Interface Anal.*, 2000, **29**, 377–380.

61 Y. Liang and W. Lu, *J. Mater. Sci. Mater. Electron.*, 2020, **31**, 17075–17083.

62 T. Muraliganth, A. V. Murugan and A. Manthiram, *Chem. Commun.*, 2009, **0**, 7360–7362.

63 T. Wang, Z. Jiang, K. H. Chu, D. Wu, B. Wang, H. Sun, H. Y. Yip, T. An, H. Zhao and P. K. Wong, *ChemSusChem*, 2018, **11**, 1365–1373.

64 W. Luo, C. Jiang, Y. Li, S. A. Shevlin, X. Han, K. Qiu, Y. Cheng, Z. Guo, W. Huang and J. Tang, *J. Mater. Chem. A*, 2017, **5**, 2021–2028.

65 B. G. Kim, J. Park, W. Choi, D. S. Han, J. Kim and H. Park, *Appl. Catal. B Environ.*, 2021, **283**, 119608.

66 T. Yamashita and P. Hayes, *Appl. Surf. Sci.*, 2008, **254**, 2441–2449.

67 C. Long, L. Jiang, T. Wei, J. Yan and Z. Fan, *J. Mater. Chem. A*, 2014, **2**, 16678–16686.

68 M. C. Biesinger, B. P. Payne, A. P. Grosvenor, L. W. M. Lau, A. R. Gerson and R. St. C. Smart, *Appl. Surf. Sci.*, 2011, **257**, 2717–2730.

69 A. Bak, W. Choi and H. Park, *Appl. Catal. B Environ.*, 2011, **110**, 207–215.

View Article Online
DOI: 10.1039/D6YA00012F

70 Z. Cai, D. Zhou, M. Wang, S.-M. Bak, Y. Wu, Z. Wu, Y. Tian, X. Xiong, Y. Li, W. Liu, S. Siahrostami, Y. Kuang, X.-Q. Yang, H. Duan, Z. Feng, H. Wang and X. Sun, *Angew. Chem. Int. Ed.*, 2018, **57**, 9392–9396.

71 R. Pai, A. Singh, S. Simotwo and V. Kalra, *Adv. Eng. Mater.*, 2018, **20**, 1701116.

72 A. P. Grosvenor, B. A. Kobe and N. S. McIntyre, *Surf. Sci.*, 2004, **572**, 217–227.

73 A. Barbieri, W. Weiss, M. A. Van Hove and G. A. Somorjai, *Surf. Sci.*, 1994, **302**, 259–279.

74 T. Fujii, F. M. F. de Groot, G. A. Sawatzky, F. C. Voogt, T. Hibma and K. Okada, *Phys. Rev. B*, 1999, **59**, 3195–3202.

75 W. Lu, Y. Shen, A. Xie and W. Zhang, *J. Magn. Magn. Mater.*, 2010, **322**, 1828–1833.

76 M. Khan, N. Shahzad, C. Xiong, T. K. Zhao, T. Li, F. Siddique, N. Ali, M. Shahzad, H. Ullah and S. A. Rakha, *Diam. Relat. Mater.*, 2016, **61**, 32–40.

77 Q. Wu, R. Zhao, X. Zhang, W. Li, R. Xu, G. Diao and M. Chen, *J. Power Sources*, 2017, **359**, 7–16.

78 M. Yu, L. Sun and X. Ning, *J. Alloys Compd.*, 2021, **878**, 160359.

79 Y. Yan, X. Lu, Y. Li, J. Song, Q. Tian, L. Yang and Z. Sui, *J. Alloys Compd.*, 2022, **899**, 163342.

80 R. Kumar, R. K. Nekouei and V. Sahajwalla, *Ceram. Int.*, 2025, **51**, 12312–12320.

81 X. Hu and J. C. Yu, *Chem. – Asian J.*, 2006, **1**, 605–610.

82 X. Chen, X. Wang and D. Fang, *Fuller. Nanotub. Carbon Nanostructures*, 2020, **28**, 1048–1058.

83 L. Li, A. Kovalchuk, H. Fei, Z. Peng, Y. Li, N. D. Kim, C. Xiang, Y. Yang, G. Ruan and J. M. Tour, *Adv. Energy Mater.*, 2015, **5**, 1500171.

84 J.-L. Hazemann, J. F. Bérar and A. Manceau, in *Materials Science Forum*, Trans Tech Publications, Ltd., 1991, vol. 79, pp. 821–826.

85 A. A. Claassen, *Proc. Phys. Soc. Lond.*, 1925, **38**, 482.

86 A. Chouchaine, S. Kouass, F. Touati, N. Amdouni and H. Dhaouadi, *J. Aust. Ceram. Soc.*, 2021, **57**, 469–477.

87 C. D. Wessels, R. A. Huggins and Y. Cui, *Nat. Commun.*, 2011, **2**, 550.

88 K. Lu, D. Li, X. Gao, H. Dai, N. Wang and H. Ma, *J. Mater. Chem. A*, 2015, **3**, 16013–16019.

89 Z. Chen, V. Augustyn, X. Jia, Q. Xiao, B. Dunn and Y. Lu, *ACS Nano*, 2012, **6**, 4319–4327.

90 L. Su, J. Winnick and P. Kohl, *J. Power Sources*, 2001, **101**, 226–230.

91 X. Tang, R. Jia, T. Zhai and H. Xia, *ACS Appl. Mater. Interfaces*, 2015, **7**, 27518–27525.

92 J. Zhu, Q. Zhang, S. Yang, L. Chen, P. Zhao and Q. Yan, *ChemElectroChem*, 2021, **8**, 4817–4825.

93 R. Li and J. Liu, *Electrochimica Acta*, 2014, **120**, 52–56.

94 H. Yin, C. Song, Y. Wang, S. Li, M. Zeng, Z. Zhang, Z. Zhu and K. Yu, *Electrochimica Acta*, 2013, **111**, 762–770.

95 J. Xie, Y. Zhu, N. Zhuang, H. Lei, W. Zhu, Y. Fu, M. S. Javed, J. Li and W. Mai, *Nanoscale*, 2018, **10**, 17092–17098.

96 H. He, D. Huang, Y. Tang, Q. Wang, X. Ji, H. Wang and Z. Guo, *Nano Energy*, 2019, **57**, 728–736.

97 J. Sun, P. Zan, X. Yang, L. Ye and L. Zhao, *Electrochimica Acta*, 2016, **215**, 483–491.

98 M. Rezapour, *Anal. Bioanal. Electrochem.*, 2018, **10**, 450–464.

99 D. Muthu, T. Sadhasivam and T. Hwan Oh, *Mater. Sci. Eng. B*, 2024, **299**, 116972.

100 N. Sinan and E. Unur, *Mater. Chem. Phys.*, 2016, **183**, 571–579.

101 Z. Cheng, T. Du, L. Zhou, H. Wang and L. Cao, *J. Colloid Interface Sci.*, 2025, **700**, 138347.

102 H. Wang, Y. Ma and W. Zhang, *Nanomaterials*, 2021, **11**, 2203.

103 S.-Y. Wang, K.-C. Ho, S.-L. Kuo and N.-L. Wu, *J. Electrochem. Soc.*, 2005, **153**, A75.

104 J. Yu, B. Wang, Q. Lu, L. Xiao, X. Ma, Y. Feng and Y. Qian, *Electrochimica Acta*, 2022, **427**, 140843.

105 G. Bharath, K. Rambabu, F. Banat, A. Hai, A. F. Arangadi and N. Ponpandian, *Sci. Total Environ.*, 2019, **691**, 713–726.

106 Q. Liu, D. Mao, C. Chang and F. Huang, *J. Power Sources*, 2007, **173**, 538–544.

107 F. I. Saaid, M. F. Kasim, C.-C. Yang, A. Kumar, T.-Y. Tseng and T. Winie, *J. Mater. Sci. Mater. Electron.*, 2022, **33**, 3648–3669.

108 T. Yang, Z. Huang, Y. Liu, M. Fang, X. Ouyang and M. Hu, *Ceram. Int.*, 2014, **40**, 11975–11983.

109 In *The Iron Oxides*, John Wiley & Sons, Ltd, 2003, pp. 1–7.

110 N. K. Chaudhari and J.-S. Yu, *J. Phys. Chem. C*, 2008, **112**, 19957–19962.

111 M. Lin, H. R. Tan, J. P. Y. Tan and S. Bai, *J. Phys. Chem. C*, 2013, **117**, 11242–11250.

112 *Handbook of Hydrothermal Technology*, Elsevier, 2013.

113 F. Zhu, J. Gao, X. Chen, M. Tong, Y. Zhou and J. Lu, *Ind. Eng. Chem. Res.*, 2015, **54**, 9072–9080.

114 F. Xu, Y. Lu, L. Sun and L. Zhi, *Chem. Commun.*, 2010, **46**, 3191–3193.

115 T. Maki, H. Kura, H. Ishida, T. Kaneko, R. Hatakeyama, M. Takahashi and T. Ogawa, *J. Phys. Conf. Ser.*, 2011, **266**, 012120.

View Article Online
DOI: 10.1039/D6YA00012F

Data availability statement

All relevant data supporting the findings of this study are included within the article and its supplementary information files.